Electronic Supplementary Material (ESI) for Journal of Materials Chemistry A.
This journal is © The Royal Society of Chemistry 2021

Electronic Supplementary Information

Unavoidable but Minimizable Microdefects in a Polycrystalline Zeolite Membrane: Its Remarkable Performance for Wet CO_2/CH_4 Separations

Yanghwan Jeong,[a] Minseong Lee,[a] Gihoon Lee,[a]
Sungwon Hong,[a] Eunhee Jang,[a] Nakwon Choi,[b,c] and Jungkyu Choi*[a]

[a.] Department of Chemical & Biological Engineering, College of Engineering, Korea University,
145 Anam-ro, Seongbuk-gu, Seoul 02841, Republic of Korea
[b.] Center for BioMicrosystems, Brain Science Institute, Korea Institute of Science and Technology (KIST),

Hwarang-ro 14-gil, Seongbuk-gu, Seoul 02792, Republic of Korea
[c.] KU-KIST Graduate School of Converging Science and Technology, Korea University,
145 Anam-ro, Seongbuk-gu, Seoul 02841, Republic of Korea

* Corresponding author

E-mail address: jungkyu_choi@korea.ac.kr, Phone: +82-2-3290-4854, and Fax: +82-2-926-6102

Table of Contents

S1. Experimental procedures

S1.1. Synthesis of heterogeneous particles

SSZ-13 particles (S-P, where S and P indicate SSZ-13 zeolites and the form of particles, respectively) were synthesized and further calcined based on detailed experimental procedures reported in our previous study.[1] The average size of S-P was ~230 nm. Subsequently, calcined S-P particles were hydrothermally grown with a synthetic precursor that enabled the synthesis of ZSM-58 zeolites; that is, the growth of calcined S-P particles with the ZSM-58 synthetic precursor containing methyltropinium iodide (MTI) as an organic structure directing agent (OSDA) according to a previously reported method.[2] The final molar composition of the ZSM-58 synthetic precursor was 23 NaOH: 70 SiO_2: 2800 H_2O: 17.5 MTI. For seeded growth, ~0.03 g of calcined S-P was added to ~30 mL of the prepared ZSM-58 synthetic precursor, and the mixture was sealed in a Teflon lined stainless-steel autoclave. Subsequently, a hydrothermal reaction was carried out in a preheated oven (PL_HV_250, Pluskolab, South Korea) at 130 °C for 10 d while the mixture was rotated at ~45 rpm. The autoclave was then quenched with tap water to stop the reaction. The resulting suspension was transferred to a conical centrifuge tube (Falcon, 50 mL) with deionized (DI) water. Subsequently, the suspension was centrifuged (Combi-514R, Hanil Science Industrial, South Korea) for 20 min. The aqueous part, expect for the white solid in the conical centrifuge tube, was discarded. Fresh DI water was replenished in the conical centrifuge tube. This process was repeated five times to wash the particles thoroughly. The solid particles were recovered and dried in an oven (HB-502M, Pluskolab, South Korea) at 70 °C. For convenience, these dried particles are considered as as-synthesized and referred to as SZ-P, where Z indicates the ZSM-58 zeolite used for seeded growth.

S1.2. Synthesis of heteroepitaxially grown zeolite films

First, calcined S-P particles were deposited on a porous α-Al_2O_3 disc to form a uniform seed layer. Approximately 30 mL of the ZSM-58 synthetic precursor used to synthesize SZ-P was added to a Teflon liner, wherein the calcined seed layer was placed in a tilted position with the seeded side facing downward. Subsequently, the liner was sealed in a stainless-steel autoclave, which was transferred to a preheated 130 °C oven (PL_HV_250, Pluskolab, South Korea), and the hydrothermal reaction was conducted under static conditions for 10 d. Detailed information regarding the preparation of the S-P seed layer and the heteroepitaxially grown zeolite film can be found in a previous study.[1] For convenience, the resulting, dried heteroepitaxially grown zeolite film is considered as as-synthesized and referred to as SZ, where S and Z are identical to those in SZ-P except that SZ is a film made on the α-Al_2O_3 disc.

S1.3. Heterogeneous particles and films calcined under various conditions

The SZ-P and SZ samples were calcined under three different conditions. First, the SZ-P and SZ samples were calcined at 550 °C for 12 h in air flowing at 200 mL·min^{-1} in a box furnace (CRF-M20-UP, Pluskolab, South Korea). For convenience, the calcined SZ-P and SZ samples are referred to as SZ-P_air and SZ_air, respectively, where the calcination environment (here, air) is appended. Second, the SZ-P and SZ samples were calcined at 450 °C for 80 h in oxygen (O_2) flowing at 200 mL·min^{-1} in the box furnace. For convenience, the resulting samples are referred to as SZ-P_O_2 and SZ_O_2, respectively, where the calcination environment of O_2 is appended. Finally, the SZ-P and SZ samples were calcined at 250 °C for 40 h in ozone (O_3) in a tubular furnace (a quartz tube with an outer diameter of 50 mm and a wall thickness of 2 mm was used). For convenience, the resulting SZ-P and SZ samples are referred to as SZ-P_O_3 and SZ_O_3, respectively, where O_3 is appended to represent the ozone calcination condition. For the ozone-based calcination, a 5 vol% ozone flow was generated by flowing pure O_2 (99.9%) at 1,000 mL·min^{-1} through an ozone generator (OZE-020, Ozone Engineering Co., Ltd., South Korea). The particle and film samples were heated at 1 and 0.2 °C·min^{-1}, respectively. For convenience, the calcined SZ particles and SZ membranes (SZ-P_*x* and SZ_*x*; *x* = air, O_2, and O_3) are called as the SZ-P particle and SZ membrane series, respectively.

S1.4. Separation performance measurements

The CO_2/CH_4 and CO_2/N_2 separation performances of the SZ membrane series were measured using the Wicke-Kallenbach method, wherein the total pressures on both the feed and permeate sides were maintained at ~1 atm. The partial pressures of the equimolar CO_2/CH_4 and CO_2/N_2 binary mixtures were approximately 51:51 (kPa/kPa) under dry conditions (referred to as DRY CO_2:CH_4 = 50:50 and DRY CO_2:N_2 = 50:50, respectively). In addition, under wet conditions, the partial pressures of the CO_2/CH_4 and CO_2/N_2 binary mixtures and water vapor were ca. 49:49:3 (kPa/kPa/kPa) (referred to as WET CO_2:CH_4 = 50:50 and WET CO_2:N_2 = 50:50, respectively). Furthermore, a flue gas showing a composition similar to that produced in coal-fired power plants[3-6] was simulated and employed to evaluate the CO_2/N_2 separation performance of the SZ membrane series. Specifically, the partial pressures of the CO_2/N_2 binary mixture were approximately 15:86 (kPa/kPa) under dry conditions (referred to as DRY CO_2:N_2 = 15:85). Under wet conditions, the partial pressures of the CO_2/N_2 mixture and water vapor were ca. 15:84:3 (kPa/kPa/kPa) (referred to as WET CO_2:N_2 = 15:85). In addition, the separation performances were measured for equimolar CO_2/CH_4 mixture and CO_2/N_2 binary mixture composed of 15% CO_2 and 85% N_2 while varying the relative humidities of the water vapor. Gas chromatographs (GCs) were used to analyze the molar fluxes of the mixtures for the SZ membrane series. Two GCs of YL 6500 (Young In Chromass, South Korea) and YL 6100 (Young In Chromass, South Korea) were used to measure the CO_2/CH_4 and CO_2/N_2 separation performances, respectively.

S1.5. Fluorescence confocal optical microscopy analysis

The defect structures in SZ_x (x = air, O_2, or O_3) were investigated using fluorescence confocal optical microscopy (FCOM). Specifically, the FCOM images were acquired using a ZEISS LSM 700 confocal microscope with a solid-state laser operating at a 555-nm wavelength. For the FCOM images, fluorescein sodium salt (F6377, Sigma-Aldrich), with molecular size of approximately 1 nm,[7] was used for dyeing the SZ membrane series because the dye molecule is smaller than the defect sizes in the zeolite membranes and larger than the pores in the DDR zeolite (0.36×0.44 nm^2).[8] In preparation for the FCOM analysis, SZ_x (x = air, O_2, or O_3) was dyed with the 1 mM fluorescein sodium salt solution. Specifically, the membrane surface was contacted with the dye solution for 4 d to allow sufficient penetration of the dye molecules into the membrane. The detailed dyeing procedure based on an osmosis-type module is described in a previous study.[9] Then, top view FCOM images of the dyed SZ membrane series were obtained from the membrane outer surface to the interface between the membrane and the α-Al_2O_3 support at an interval of ~0.25 μm.

The resulting FCOM images were further used to quantitatively estimate the properties (mainly the area fraction and tortuosity) of the defect structures by image processing. In addition, the quantitative properties of the defect structures were complemented with unidimensional permeation modeling. This combination yielded the porosity (or density) and size (or width) of the defects. Simultaneously, we could attribute the contributions of the defective and zeolitic parts to the final molar flux of the CO_2 molecules. Detailed information regarding the quantitative analysis of the defects and the contributions of the defective and zeolitic parts to the final CO_2 molar flux has been provided in previous studies.[10, 11] In addition, to estimate the rates of CO_2 permeation inhibited by the adsorbed water molecules, we considered the linear combination of permeations by water-molecule-induced defect blockage and outer and inner surface inhibitions. Detailed information about distinguishing the contributions of the defect blockage and surface inhibitions can be found elsewhere.[12] In this study, we further decoupled the surface inhibitions by considering the water-molecule-induced permeation resistance on the membrane outer surface (called the outer surface inhibition) and on the inner micropore surface inside the zeolite membrane (called the inner surface inhibition). For this, we estimated the two surface inhibitions according to the Boltzmann-equation-based statistical approach as follows:

$$y = \frac{A_1 - A_2}{1 + e^{(x - x_0)/dx}} + A_2.$$

For simplicity, we assumed that the CO_2 permeation reduced by the outer surface inhibition was determined at a very low water vapor pressure (i.e., the y-axis intercept) and that reduced CO_2 permeation rate because of inner surface inhibition gradually increased with the increasing content of water molecules adsorbed inside the micropores.

S1.6. Characterization

Scanning electron microscopy (SEM) images and energy dispersive X-ray spectroscopy (EDX) results were obtained using a Hitachi S-4800 field emission-scanning electron microscope (FE-SEM). In addition, SEM images of calcined S-P were obtained using a Hitachi S-4300 FE-SEM. For the SEM images, the particle and membrane samples were precoated with platinum by a Hitachi-1045 ion sputter. A Rigaku Model D/Max-2500V/PC diffractometer equipped with a Cu K_α radiation source (λ = 0.154 nm) was used to obtain the X-ray diffraction (XRD) patterns of the particle and membrane samples. For comparison, the simulated XRD patterns of the all-silica CHA and DDR zeolites were acquired using Mercury software (Cambridge Crystallographic Data Centre; CCDC). The corresponding crystallographic information files (CIFs) were downloaded from the International Zeolite Association (IZA) website (http://www.iza-online.org). Thermogravimetric analysis (TGA) results were obtained using a Q50 (TA Instruments, USA) in air and O_2. Weight loss percentage after calcination of SZ-P in air, O_2, and O_3 was obtained by the batch-wise calcination in box (calcination in air and O_2) and tubular (calcination in O_3) furnaces for different durations. First, a weight of SZ-P (approximately 0.1 g) was measured and then placed in a porcelain holder. The porcelain holder was transferred to the box or tubular furnace. Temperature was increased at a heating ramp rate of 10 $°C \cdot min^{-1}$ to a target temperature. After reaching the target temperature, it was held at 550 °C for up to 12 h under air, at 450 °C for up to 80 h under O_2, and at 250 °C for up to 80 h under O_3. Finally, the final weight of calcined SZ-P was measured again after different durations to calculate the weight loss percentage. Fourier transform infrared (FT-IR) spectroscopy (Nicolet^{TM} iS50, Thermo Scientific^{TM}, USA) was used to verify the presence of OSDAs in the particle and membrane samples. The FT-IR spectra of the particle and membrane samples were acquired in the transmittance and attenuated total reflectance (ATR) modes, respectively. Specifically, the SZ-P particle series were pelletized for the FT-IR measurements and mounted in an *in-situ* cell. Subsequently, the *in-situ* cell was heated at 200 °C for 12 h to remove any residual moisture and was then cooled to 150 °C under vacuum before starting the measurements. An ASAP 2020 (Micromeritics Instruments Corporation, USA) was used to measure the adsorption isotherms of CO_2, CH_4, and N_2 in SZ-P_air at 30, 50, and 75 °C for the CO_2 and CH_4 molecules and at 10, 20, and 30 °C for the N_2 molecules. In addition, the Ar physisorption isotherms at 87 K for the SZ-P particle series were obtained using the ASAP 2020. In addition, the water vapor adsorption isotherms were measured using a vapor sorption analyzer (DVS Vacuum, Surface Measurement Systems, England) at 50 °C for the SZ-P particle series. To investigate the hydrophobicity of the SZ membrane series, the contact angles of water droplets on the membrane surfaces were obtained using a contact angle analyzer (Phoenix-300, Surface Electro Optics, South Korea).

S2. Supplemental results and discussion

S2.1. Properties of the SZ particle series

Fig. S2a and b reveals the changes in weight of SZ-P at ca. 260 °C in air and at ca. 240 °C in O_2. The TGA result obtained for MTI in air indicates that MTI was oxidized at approximately 310 °C (Fig. S2c). Thus, it is reasonable to accept that the changes in weight observed in Fig. S2a and b were associated with the removal of MTI from the outer surface of SZ-P not from inside. To accurately measure the MTI content inside SZ-P, the sample was heated again at 300 °C for 3 h to remove any external residual MTI (Fig. S2d). Accordingly, the weight of MTI inside SZ-P was ~12 wt%, which was in good agreement with ca. 12 wt% of MTI inside the ZSM-58 zeolites.[2, 13] This strongly indicates that the DDR zeolites are a major constituent of SZ-P.

S2.2. Properties of the SZ membrane series

We investigated the membrane properties of SZ and SZ_*x* (*x* = air, O_2, and O_3). The top and cross-sectional view SEM images and water contact angles are shown in Fig. S6. In the top view SEM images in Fig. S6a1-d1, the shapes and sizes of the grains among SZ and SZ_*x* (*x* = air, O_2, and O_3) were indistinguishable, indicating that the membrane constituents were negligibly affected by the different calcination methods. The EDX results of the Si and Al atoms shown in Fig. S6a2-d2 indicate the plausible high hydrophobicity of all the SZ membrane series. The SZ membrane series were ~7 μm thick, which is in good agreement with previously reported membrane thickness.[1] In addition, although some Al atoms leached from the α-Al_2O_3 discs during the secondary growth can be incorporated into some parts near the interface,[14, 15] the majority of the membrane constituents in the SZ membrane series were highly siliceous and plausibly hydrophobic, provided that they were fully calcined (Fig. S6b2-d2). Along with the EDX result, the water droplet contact angles shown in Fig. S6b3-d3 confirm the high hydrophobicity of the SZ membrane series. In contrast, the as-synthesized SZ film exhibited some hydrophilic properties (Fig. S6a3), which could be related to the water-soluble MTI included in the ZSM-58 precursor. Furthermore, the XRD patterns of SZ_*x* (*x* = air, O_2, and O_3) shown in Fig. S7 reveal that the major constituent of the hybrid membrane was the DDR zeolite, while the SSZ-13 zeolite originating from the seed layer was a minor constituent.

S2.3. CO_2/N_2 separation performances of the SZ membrane series

The CO_2/N_2 separation performances of the SZ membrane series under both dry and wet conditions are shown in Fig. S9. Specifically, the maximum CO_2/N_2 SFs were 16.2 ± 1.2 for SZ_air (Fig. S9a1), 18.0 ± 2.5 for SZ_O_2 (Fig. S9b1), and 29.2 ± 0.1 for SZ_O_3 (Fig. S9c1) at 30 °C under dry conditions. However, the CO_2/N_2 SFs at 50 °C (a representative temperature of the flue gas emitted from coal-fired power plants) under wet conditions were 14.4 ± 4.0 for SZ_air (Fig. S9a2), 17.9 ± 4.2 for SZ_O_2 (Fig. S9b2), and 14.7 ± 2.4 for SZ_O_3 (Fig. S9c2). In general, the trends of the CO_2 and N_2 permeances observed under dry and wet conditions were similar to those observed for the equimolar CO_2/CH_4 mixtures (Fig. 2a2-c2). However, although the kinetic diameter of CH_4 (0.38 nm) is slightly larger than that of N_2 (0.364 nm), it is relatively much larger than the 8-MR channels in the DDR zeolite (0.36×0.44 nm^2). Therefore, the molecular sieve effect was more pronounced for the CO_2/CH_4 mixtures than for the CO_2/N_2 ones, thereby resulting in the extremely high CO_2/CH_4 SFs for the SZ membrane series (~285-673 at 30 °C).

In addition, we carried out CO_2/N_2 permeation tests of the SZ membrane series for a simulated flue gas composition (Fig. S10). For the simulation, we considered the compositions of the main components (15% CO_2 and 85% N_2) and the third most abundant component, water vapor.[3-6] The resulting maximum CO_2/N_2 SFs at 30 °C under dry conditions were 16.2 ± 2.0 for SZ_air (Fig. S10a1), 18.2 ± 1.2 for SZ_O_2 (Fig. S10b1), and 28.6 ± 4.7 for SZ_O_3 (Fig. S10c1). This trend would reflect the degree of defects in the SZ membrane series, which plausibly decreased in the order SZ_air, SZ_O_2, and SZ_O_3. Notably, these values were close to those observed for the equimolar CO_2/N_2 mixtures (Fig. S9a1-c1). This was attributable to the almost linear behaviors of both the CO_2 and N_2 molecules in SZ-P_air up to ~1 bar at 30 °C (Fig. S15). In addition, introducing the water vapor to the dry feed similarly reduced the CO_2/N_2 permeances and, thus, the CO_2/N_2 SFs at 30 °C were comparable, except for that of SZ_O_3, which showed a more pronounced reduction in the CO_2 permeance and, accordingly, a very low CO_2/N_2 SF at 30 °C. Nevertheless, the CO_2/N_2 SFs at 50 °C under wet conditions were as high as 19.6 ± 1.3 for SZ_air (Fig. S10a2), 22.8 ± 2.6 for SZ_O_2 (Fig. S10b2), and 17.2 ± 3.5 for SZ_O_3 (Fig. S10c2). Despite the high

CO_2/N_2 SFs at 50 °C, the CO_2 permeances through SZ_O_3 drastically decreased, plausibly because of the hydrophilicity of the residual MTI inside the DDR zeolite: ~9×10^{-9} mol·m^{-2}·s^{-1}·Pa^{-1} for SZ_O_3 was much lower than those of both SZ_air and SZ_O_2 (~3.1-3.2×10^{-8} mol·m^{-2}·s^{-1}·Pa^{-1} at 50 °C).

In addition to the CO_2/N_2 separation performance plotted as a function of temperature (Fig. S9 and S10), the relative humidity of the water vapor was systematically increased from 0% through 26% and 60% to 100% at 50 °C to determine its effect on the CO_2/N_2 separation performance (Fig. S11a1-c1). As the relative humidity was increased, the CO_2 and N_2 permeances decreased monotonically. Interestingly, the degree of the decreased permeance was comparable for both CO_2 and N_2, as mentioned above for both SZ_air and SZ_O_2 shown in Fig. S10a1-a2 and b1-b2. Accordingly, the comparable CO_2/N_2 SFs were maintained up to 100% relative humidity. However, the effect of the water vapor on the rates of CO_2/N_2 permeation through SZ_O_3 was distinct; that is, the degree of CO_2 permeance became increasingly pronounced with increasing relative humidity, thus resulting in the monotonically decreasing CO_2/N_2 SFs. Although the apparently defect-free SZ_O_3 achieved the highest CO_2/N_2 SF under dry conditions, it showed rather weak resistance against water vapor, seemingly because of the aforementioned hydrophilicity. This indicates the importance of maximizing hydrophobicity to achieve high CO_2 permselectivities for water vapor-containing feeds. The full recovery of the CO_2/N_2 separation performance after removing the water vapor from the feed indicates the robustness of the inorganic zeolite membranes.

By determining the effect of the water vapor on the CO_2/N_2 separation performance, we further confirmed the long-term stabilities of the SZ membrane series at 100% relative humidity and 50 °C (Fig. S11a2-c2). For both SZ_air and SZ_O_2, the CO_2/N_2 SF increased from 15 and 15.6 under dry conditions to 16.2 and 22.8, respectively, at the 100% relative humidity at the expense of the reduced CO_2 permeance (Fig. S11a1-b1 and a2-b2). However, gradually adding the water vapor to the feed monotonically decreased the CO_2/N_2 SF of SZ_O_3 (Fig. S11c1 and c2) from 23.5 under dry conditions to 7.3 at 100% relative humidity. Fig. S11a2-c2 reveals that the hydrophobic SZ membranes (i.e., SZ_air and SZ_O_2) could preserve the high CO_2/N_2 SFs (~16-23) without showing any noticeable performance degradation, whereas SZ_O_3 could not feasibly maintain the original high CO_2/N_2 SF under dry conditions at 100% relative humidity. This strongly supports the desirable hydrophobicity of the zeolite membrane to ensure high CO_2 permselectivities under wet conditions. Despite the intentionally interposed hydrothermal treatment at 200 °C in Fig. S11a2-c2, the SZ membrane series could provide steady CO_2 permselectivities, thereby supporting the application of zeolite membranes.

S2.4. Comparison of the CO_2/N_2 separation performances of the SZ membrane series and other membranes

We noticed that the CO_2/N_2 separation performance of the entire SZ membrane series measured at 50 °C could not overcome the Robeson upper bound limit under both dry and wet conditions (Fig. S21a).[16] Nevertheless, SZ_O_2 still exhibited very good CO_2/N_2 SFs (ca. 22.8) at the saturated water vapor pressure of 12.3 kPa at 50 °C. Likewise, the SZ membranes series showed the high CO_2/N_2 separation performances under both dry and wet conditions, as compared to those of other zeolite membranes; (1) DDR type: ZSM-58[17] and *c*-oriented DDR,[18] (2) CHA type: SSZ-13,[19, 20] dye-post-treated SSZ-13,[10] RTP-treated SSZ-13,[12] CHA,[21] CVD-treated CHA,[22] and SDA-free CHA,[23] and (3) faujasite[24] zeolites (Fig. S21b). SZ_air, which comprises the majority of the ZSM-58 zeolites, showed good CO_2/N_2 separation performances comparable to those of the homogeneous ZSM-58 membrane[17] under both dry and wet conditions. Furthermore, defect-free SZ_O_3 showed a very high CO_2/N_2 SF (ca. 23.5) under dry conditions, whereas SZ_air and SZ_O_2 showed the CO_2/N_2 SFs (ca. 14.9-17.2) comparable or superior to those of intact or post-treated CHA type membranes. However, adding the water vapor to the feed resulted in good CO_2/N_2 SFs (ca. 22.8) for SZ_O_2. In particular, the hydrophobicity of a zeolite membrane constituent was required for achieving high CO_2 permselectivities under wet conditions, as reflected by the SZ_O_2 performance and the significant performance deterioration in the hydrophilic faujasite zeolite membrane.[24]

Table S1 Dual-site Langmuir adsorption constants and saturation capacities estimated from CO_2 adsorption isotherms in SZ_air and single-site Langmuir adsorption constants and saturation capacities estimated from N_2 and CH_4 adsorption isotherms in SZ_air.[25, 26]

Adsorbed gas	Temp. (°C)	Q_{sat}^A (mol·kg^{-1})	K^A (kPa^{-1}) × 10^3	-ΔH_{ads}^A (kJ·mol^{-1})	Q_{sat}^B (mol·kg^{-1})	K^B (kPa^{-1}) × 10^3	-ΔH_{ads}^B (kJ·mol^{-1})
CO_2	30	0.15 ± 0.01	33,000 ± 7,580	69.4 ± 13.3	2.69 ± 0.06	11.9 ± 0.48	33.4 ± 0.47
	50		3,290 ± 486			5.34 ± 0.18	
	75		922 ± 3			2.14 ± 0.07	
N_2	10	0.94 ± 0.01	3.51 ± 0.07	26.4 ± 1.8			
	20		2.50 ± 0.04				
	30		1.68 ± 0.03				
	50		0.89[a]				
CH_4	30	1.27 ± 0.03	4.14 ± 0.12	30.2 ± 1.8			
	50		2.13 ± 0.05				
	75		0.88 ± 0.02				

[a] Estimated based on the values measured at 10, 20, and 30 °C.

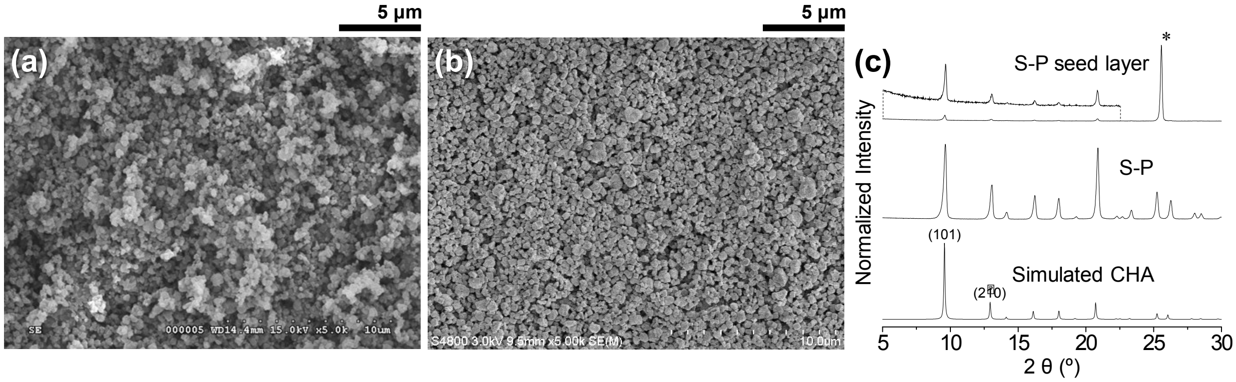

Fig. S1 SEM images of (a) calcined S-P particles and (b) a calcined seed layer comprising the S-P particles shown in (a) along with (c) the corresponding XRD patterns. A magnified XRD pattern of the S-P seed layer is shown above the normalized XRD pattern. In addition, the simulated XRD pattern of all-silica CHA zeolite is added at bottom. Finally, an asterisk (*) denotes a XRD peak originating from an α-Al_2O_3 disc.

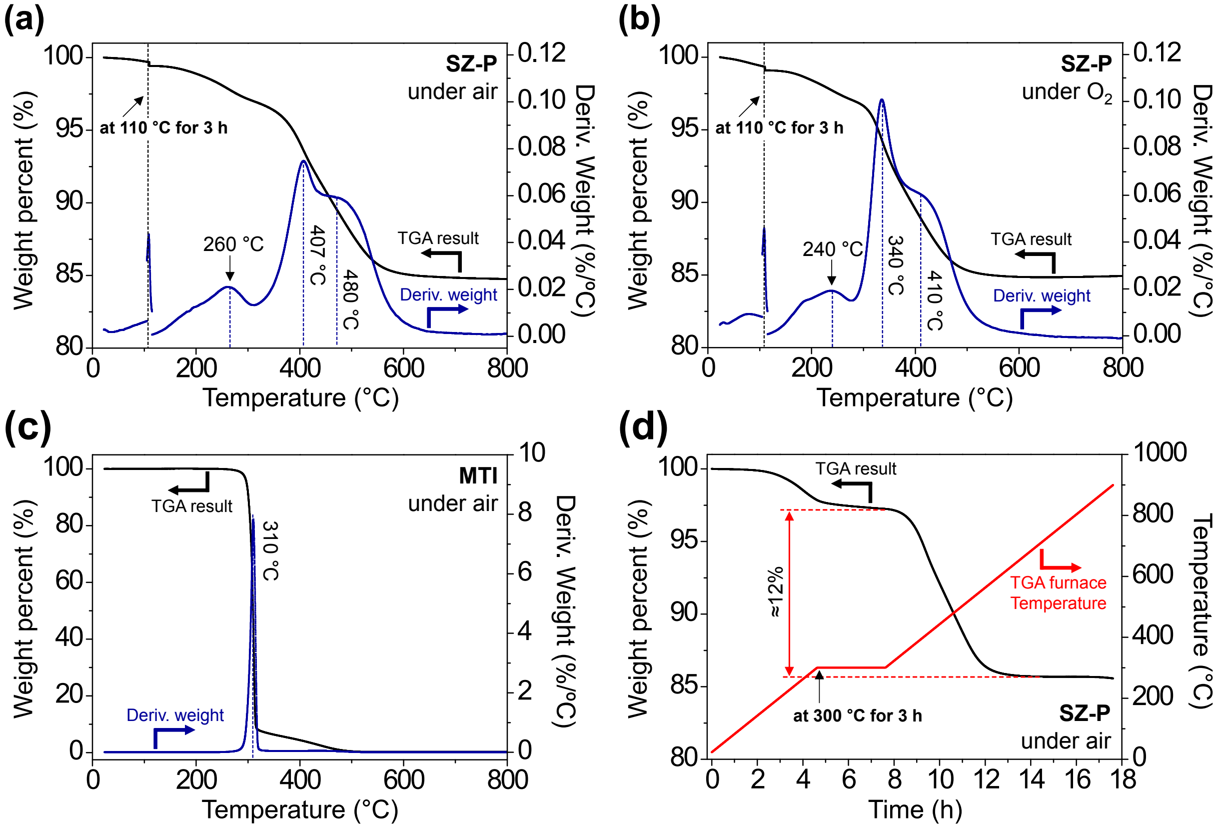

Fig. S2 Thermogravimetric analysis (TGA) and differential thermal gravimetric (DTG) curves of (a, b) SZ-P and (c) MTI in (a, c) air and (b) O_2 plotted as a function of temperature up to 800 °C. In (a, b), a black dashed line indicates heat treatment at 110 °C for 3 h to remove weakly adsorbed molecules (e.g., water molecules) from SZ-P. (d) TGA results of SZ-P in air with respect to a temperature profile (marked in red). In (a-c), the samples were heated at 1 °C·min^{-1} and blue dashed lines indicate peak positions of derivative weight loss curves.

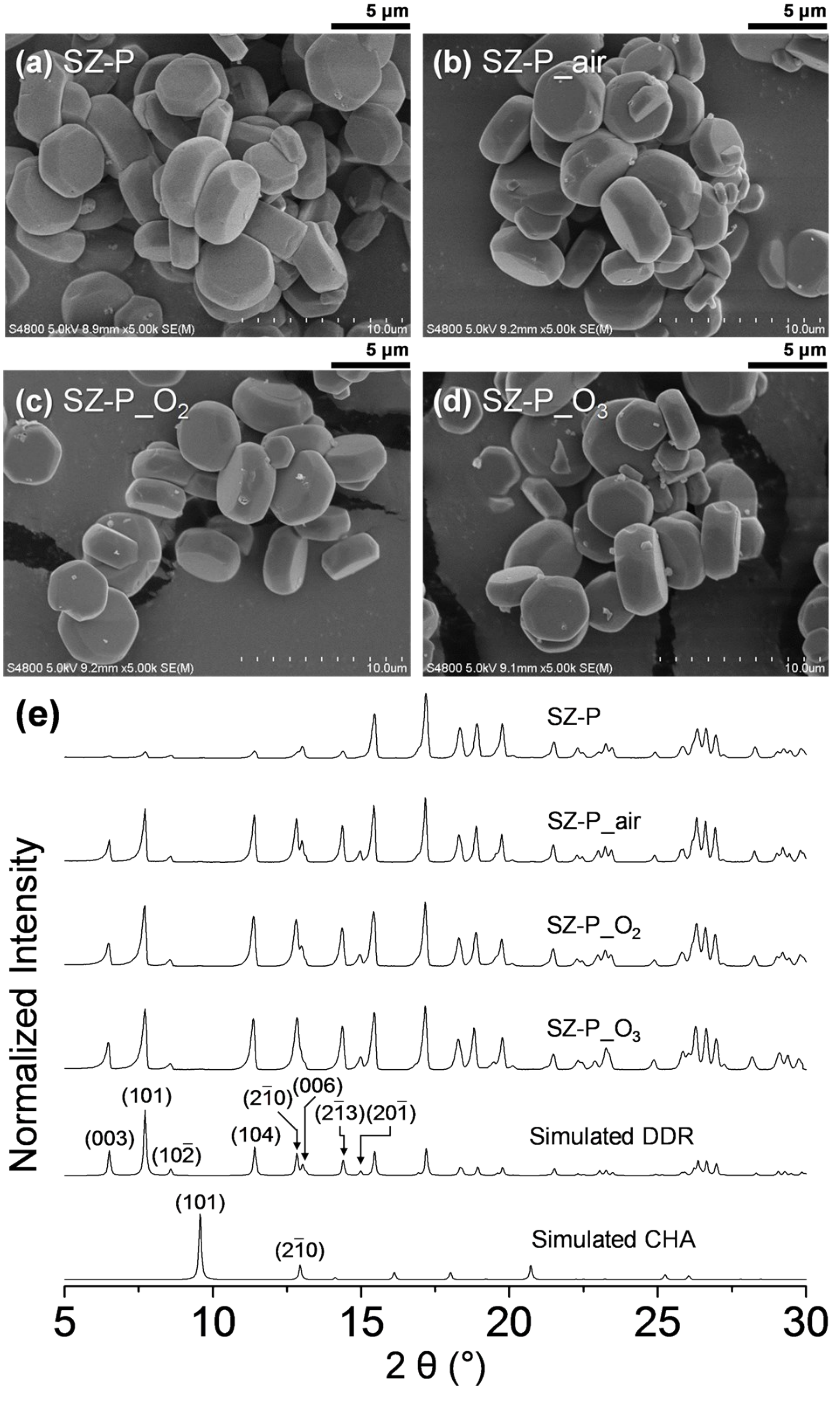

Fig. S3 SEM images of (a) SZ-P, (b) SZ-P_air, (c) SZ-P_O$_2$, and (d) SZ-P_O$_3$ along with (e) the corresponding XRD patterns. In (e), the simulated XRD patterns of all-silica CHA and DDR zeolites are provided.

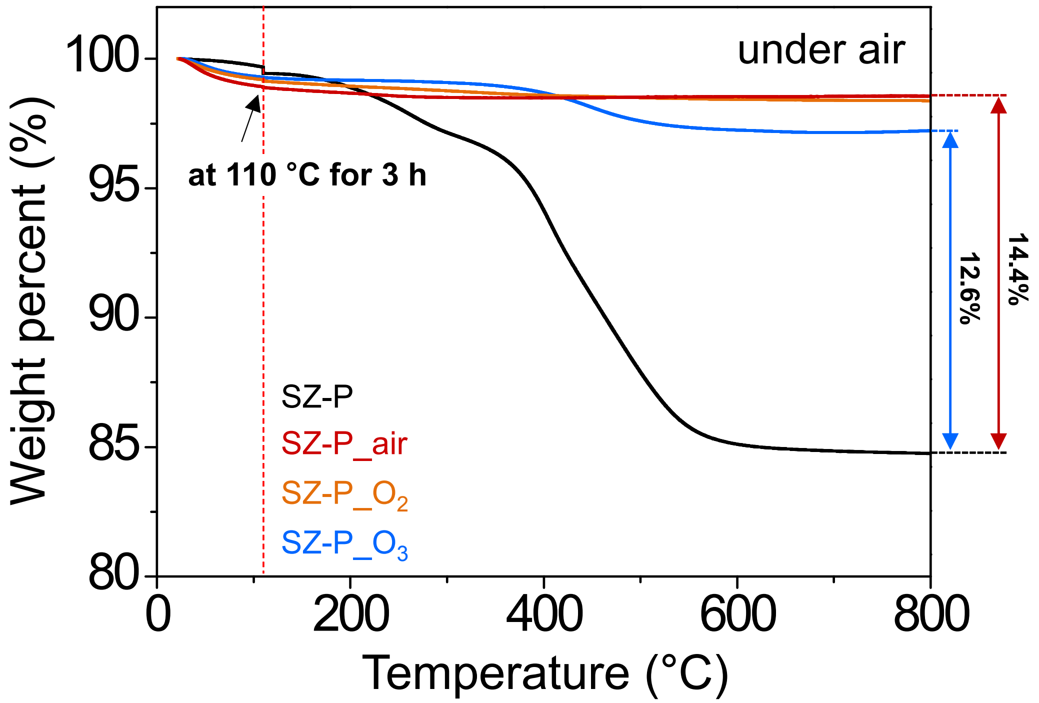

Fig. S4 TGA results of SZ-P (*black*), SZ-P_air (*red*), SZ-P_O$_2$ (*orange*), and SZ-P_O$_3$ (*blue*). TGA was measured as a function of temperature up to 800 °C at a ramp rate of 1 °C·min^{-1}. For the removal of weakly adsorbed molecules, heat treatment at 110 °C for 3 h was conducted (indicated by a red dashed line). In addition, weight loss percentage at 800 °C was calculated by setting the weight percent to 100% after the heat treatment at 100 °C (indicated by the red vertical dashed line).

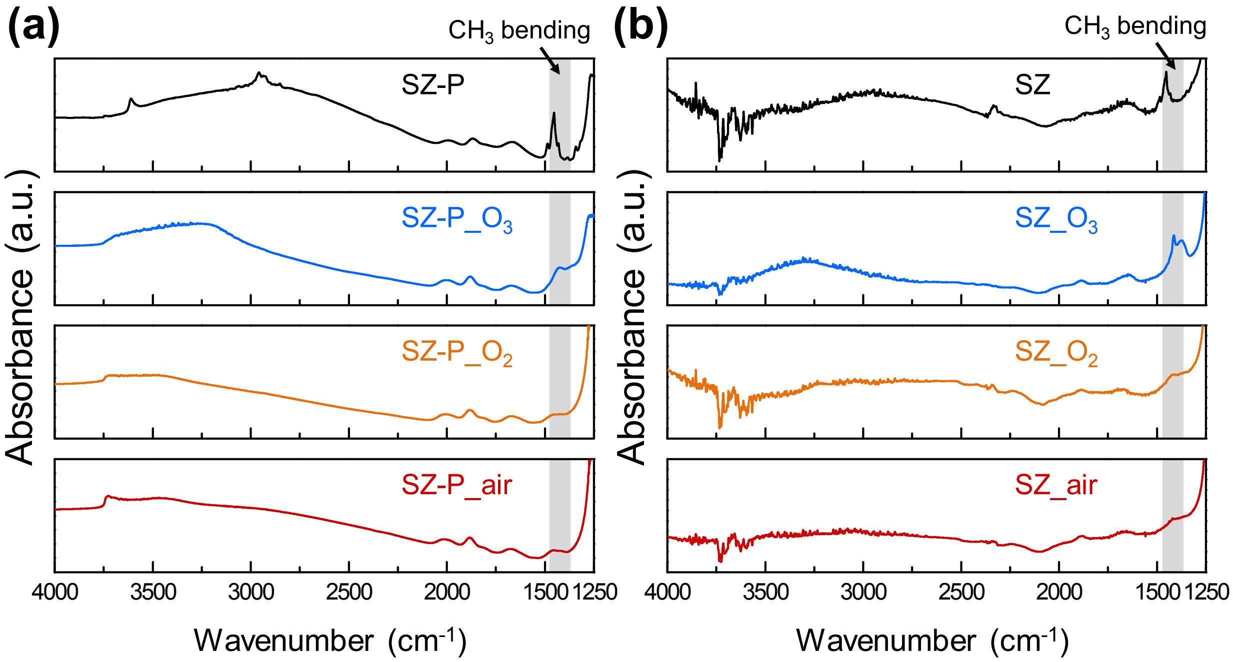

Fig. S5 FT-IR spectra of (a) SZ-P and SZ-P_*x* (*x* = air, O_2, and O_3) obtained in the transmission mode and (b) SZ and SZ_*x* (*x* = air, O_2, and O_3) obtained in the attenuated total reflection (ATR) mode. IR peak ranges due to the CH_3 bending are marked by shaded areas.

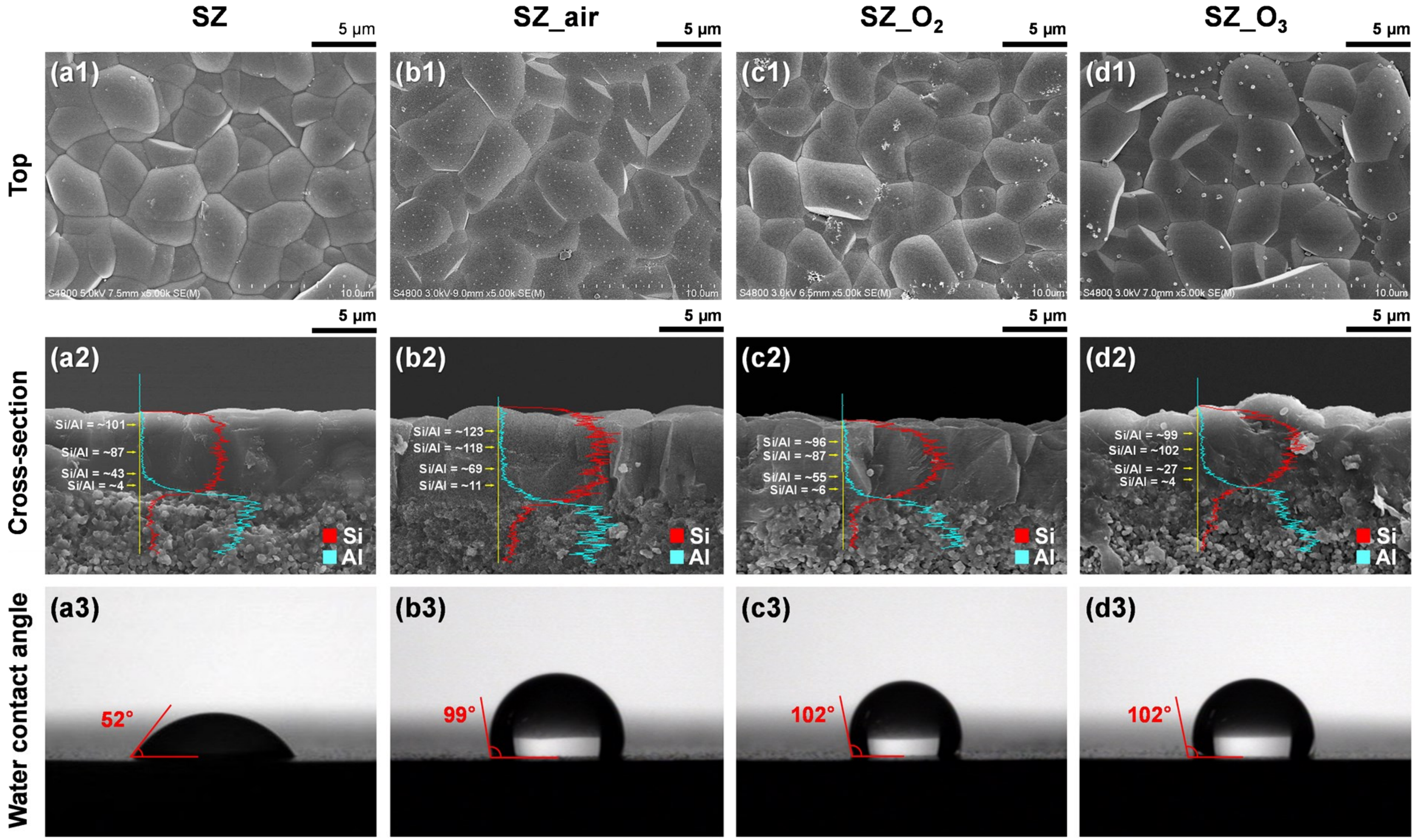

Fig. S6 (a1-d1) Top view SEM images and (a2-d2) cross-sectional view SEM images along with the EDX results for Si (*red*) and Al (*cyan*) of SZ and SZ_*x* (*x* = air, O_2, and O_3). (a3-d3) Images of contact angles measured immediately after dropping water onto membrane surfaces. (a1-a3) SZ, (b1-b3) SZ_air, (c1-c3) SZ_O_2, and (d1-d3) SZ_O_3. For better understanding, in (a2-d2), the values of Si/Al ratios estimated from the EDX results are displayed at four points (*indicated by yellow arrows*) of the cross-sectional view SEM images.

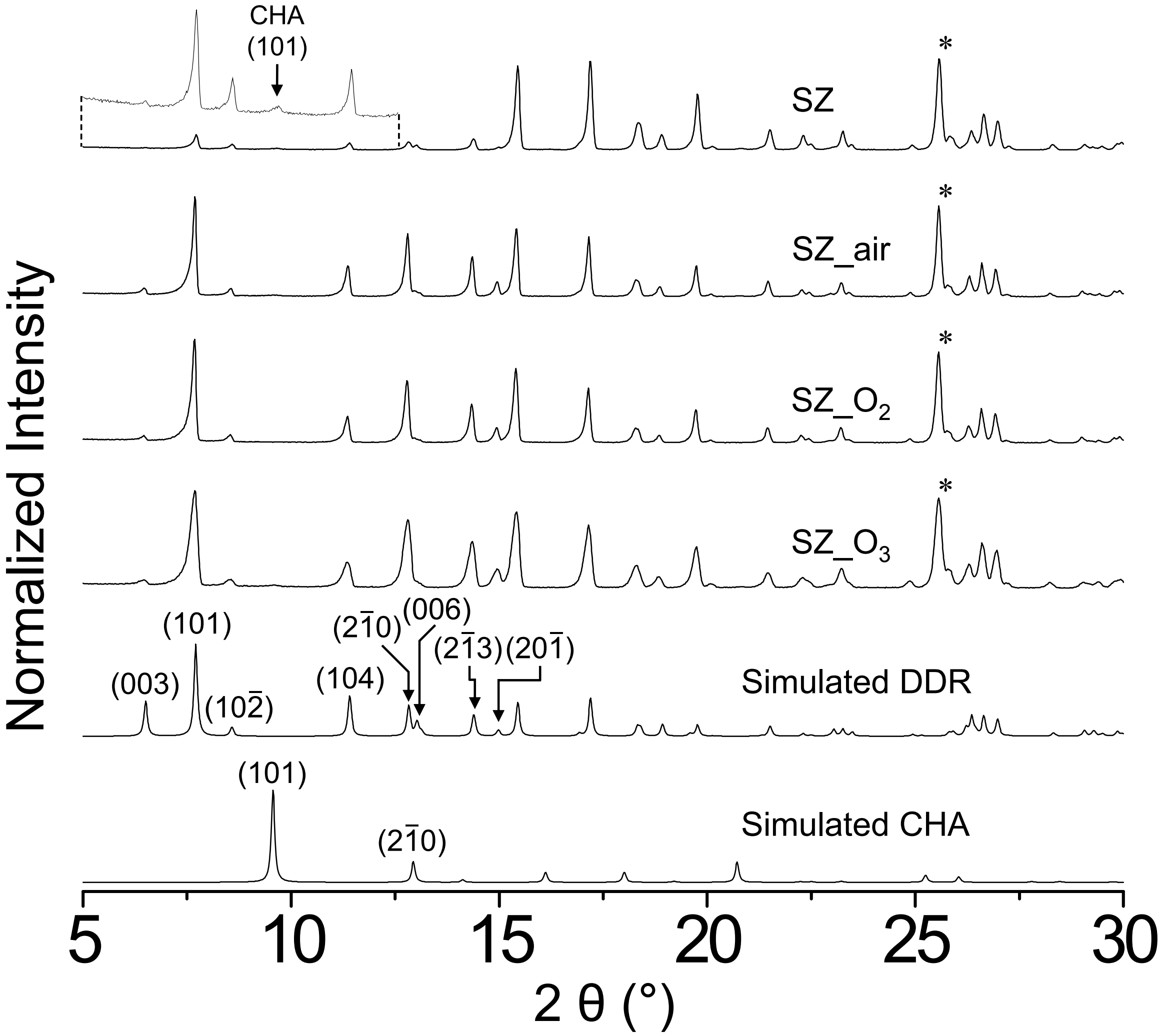

Fig. S7 XRD patterns of SZ, SZ_air, SZ_O_2, and SZ_O_3. For clarity, the magnified XRD pattern of SZ is shown above its normalized one. The simulated XRD patterns of the all-silica CHA and DDR zeolites are added at bottom. Asterisks (*) denote the XRD peaks originating from the α-Al_2O_3 disc.

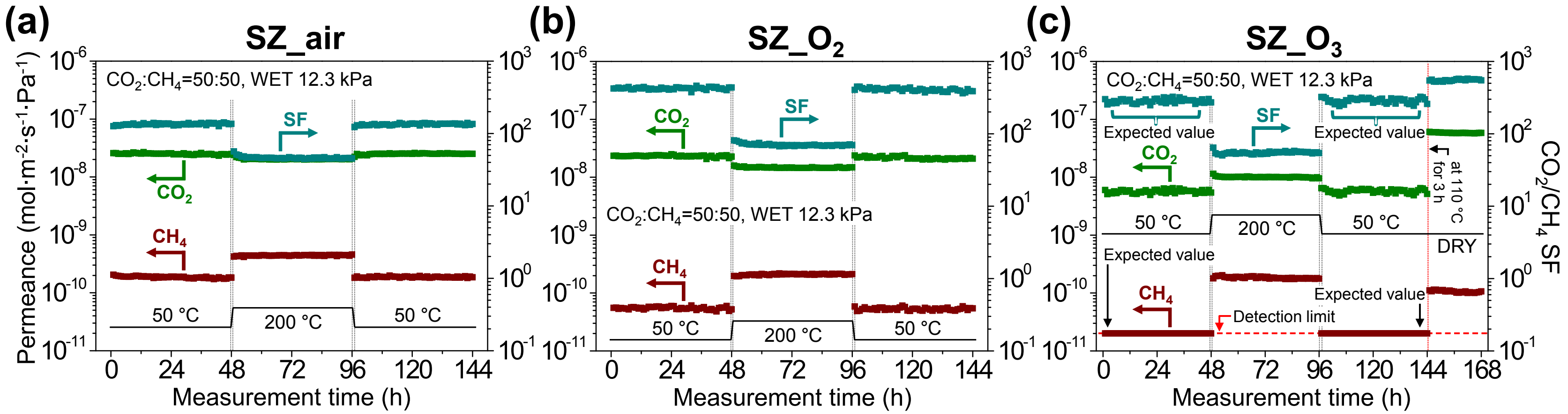

Fig. S8 Long-term stability tests of (a) SZ_air, (b) SZ_O_2, and (c) SZ_O_3 conducted at 50 °C up to 4 d to separate equimolar CO_2/CH_4 binary mixture feed containing water vapor (12.3 kPa). Harsh conditions at 200 °C for 2 d were intentionally interposed to simulate long-term use. In (c), after long-term stability test of SZ_O_3 at 12.3 kPa under wet conditions, SZ_O_3 was heated at 110 °C for 3 h and then separation performance was measured at 50 °C under dry conditions.

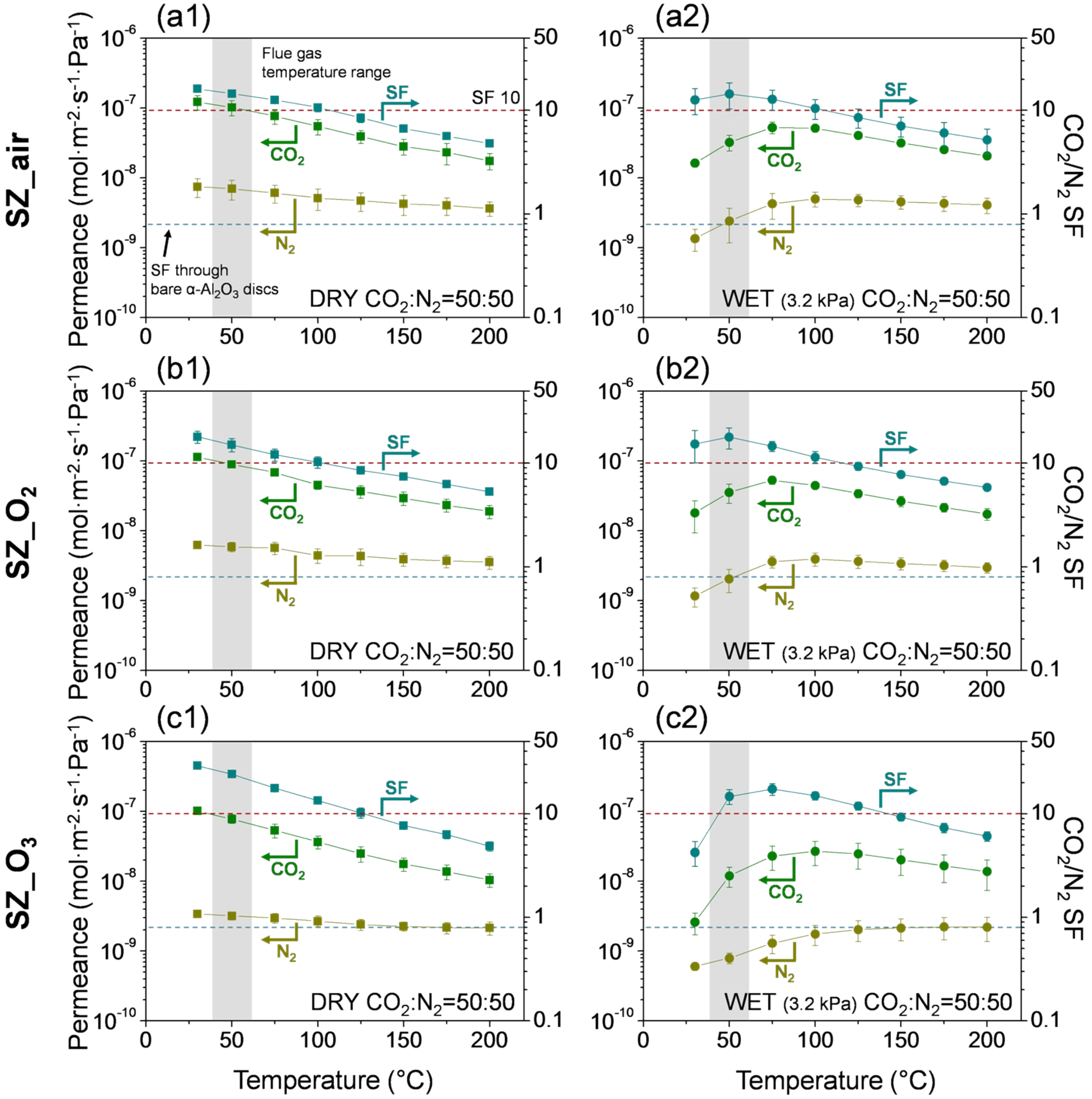

Fig. S9 CO$_2$/N$_2$ permeances and SFs of (a1, a2) SZ_air, (b1, b2) SZ_O$_2$, and (c1, c2) SZ_O$_3$ measured under both (a1-c1) dry and (a2-c2) wet conditions. Separation performances of the SZ membrane series are plotted as a function of temperature up to 200 °C for equimolar CO$_2$/N$_2$ binary mixture feed. Red and cyan dashed lines indicate the CO$_2$/N$_2$ SFs of 10 and 0.8 (the SF value through a bare α-Al$_2$O$_3$ disc), respectively. For clarity, temperature ranges of flue gases emitted from coal-fired power plants are shaded.

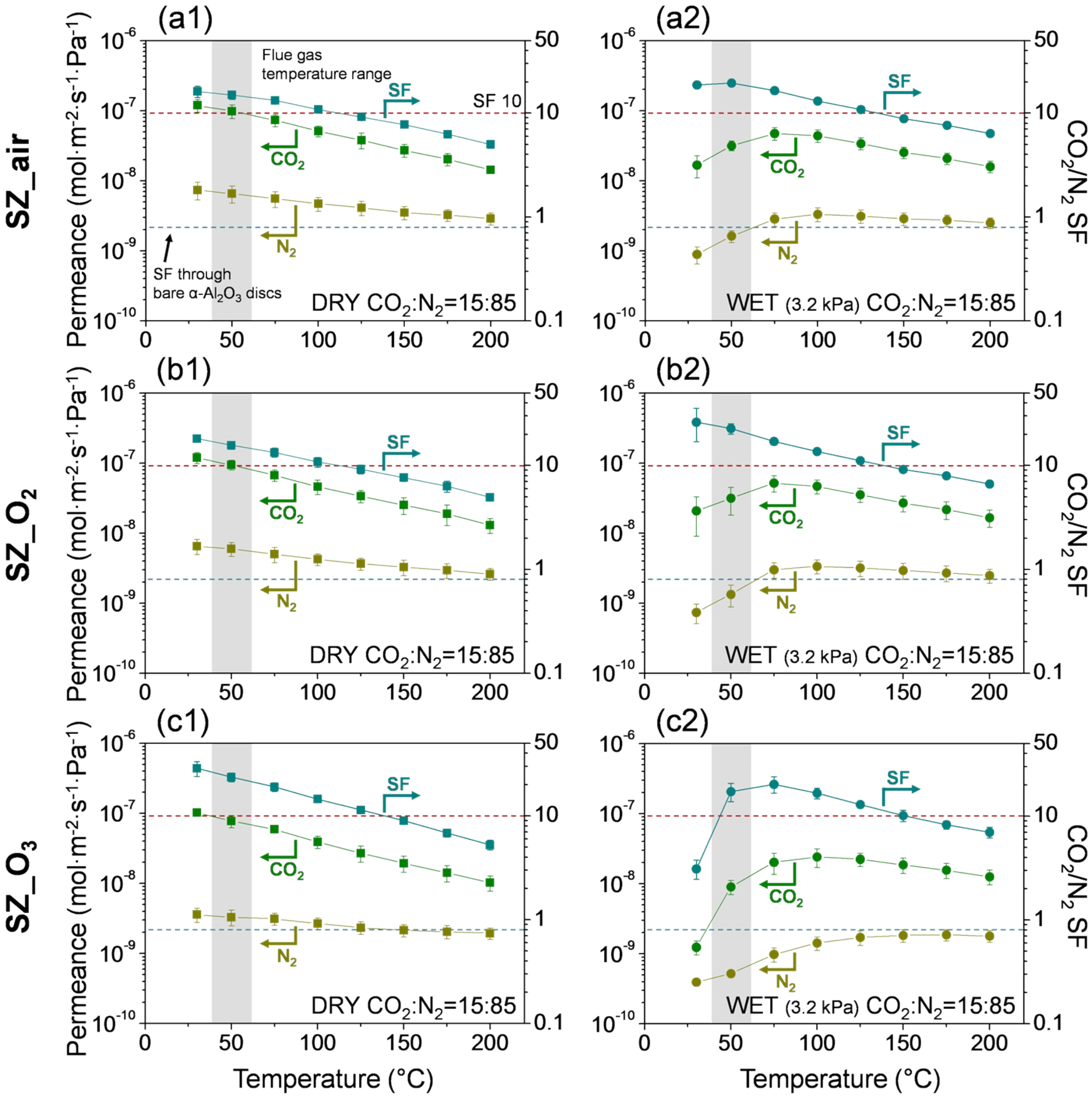

Fig. S10 CO_2/N_2 permeances and SFs of (a1, a2) SZ_air, (b1, b2) SZ_O_2, and (c1, c2) SZ_O_3 measured under both (a1-c1) dry and (a2-c2) wet conditions. Separation performances of SZ membrane series are plotted as a function of temperature up to 200 °C for binary mixture feed composed of 15% CO_2 and 85% N_2. Red and cyan dashed lines indicate the CO_2/N_2 SFs of 10 and 0.8 (the SF value through a bare α-Al_2O_3 disc), respectively. For clarity, temperature ranges of flue gases emitted from coal-fired power plants are shaded.

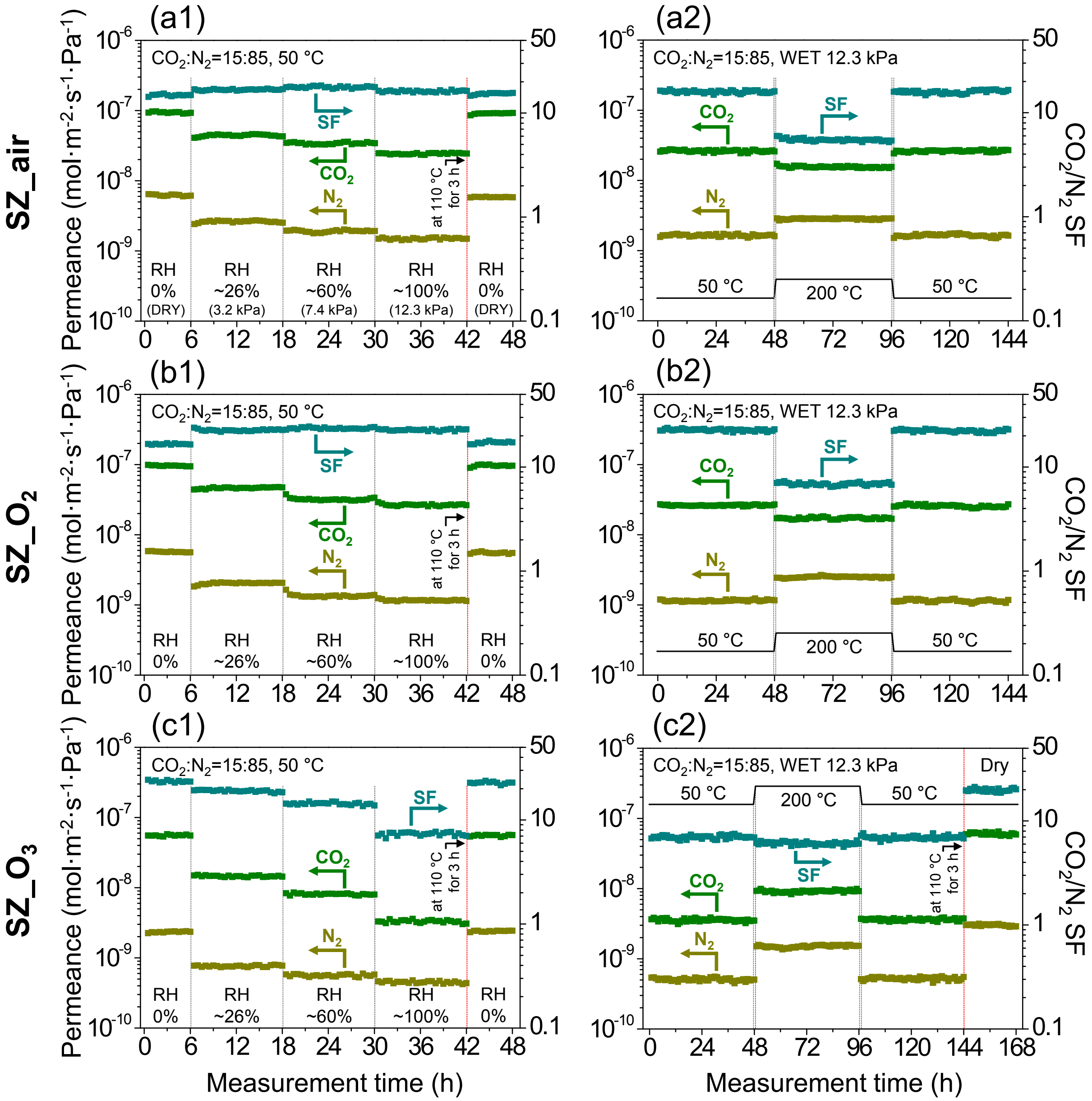

Fig. S11 Stability tests of (a1) SZ_air, (b1) SZ_O$_2$, and (c1) SZ_O$_3$ for various humidities. Relative humidity was changed from 0% through ~26% and ~60% to ~100% (corresponding to H_2O partial pressures of 0, 3.2, 7.4, and 12.3 kPa, respectively) at 50 °C in CO_2/N_2 binary mixture feed composed of 15% CO_2 and 85% N_2. Long-term stability tests of (a2) SZ_air, (b2) SZ_O$_2$, and (c2) SZ_O$_3$ conducted at 50 °C up to 4 d in CO_2/N_2 binary mixture feed composed of 15% CO_2 and 85% N_2 containing water vapor (12.3 kPa). Harsh conditions at 200 °C for 2 d were intentionally interposed to simulate long-term use. After (a1-c1) relative humidity and (c2) long-term stability tests at 12.3 kPa under wet conditions, samples were heated at 110 °C for 3 h and then separation performances were measured at 50 °C under dry conditions.

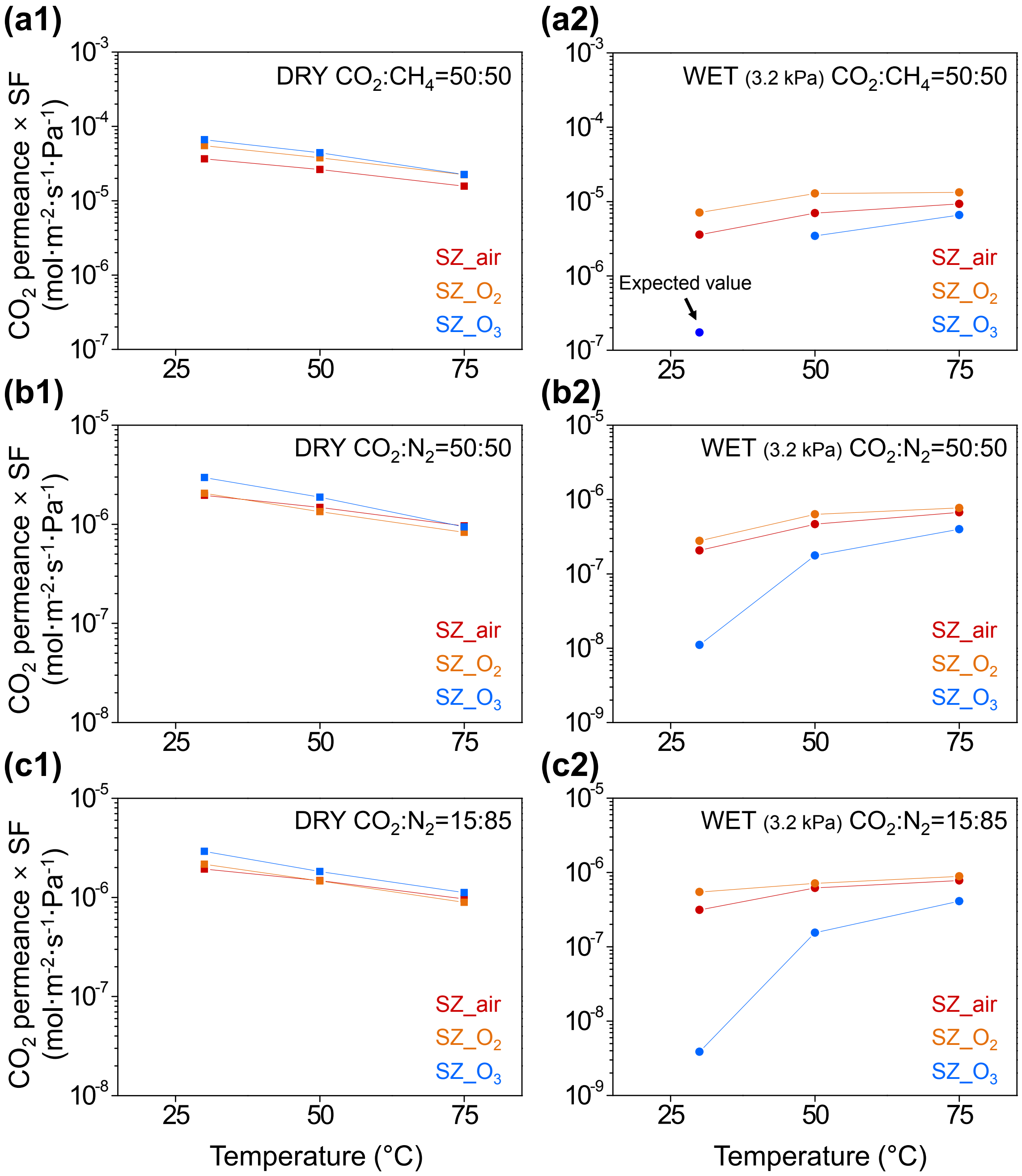

Fig. S12 CO_2 permeances × SFs of SZ_air (*red*), SZ_O_2 (*orange*), and SZ_O_3 (*blue*) measured under both dry (*left*) and wet (*right*) conditions and plotted with respect to the relevant temperature ranges for equimolar (a1, a2) CO_2/CH_4 and (b1, b2) CO_2/N_2 binary mixture feeds and (c1, c2) CO_2/N_2 binary mixture feed composed of 15% CO_2 and 85% N_2.

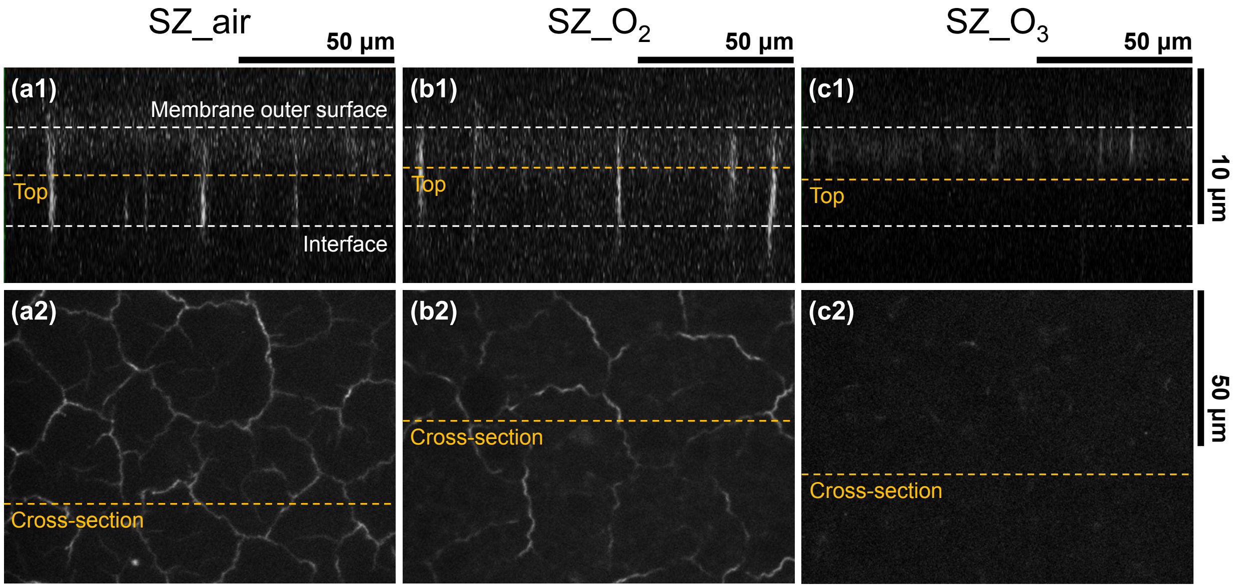

Fig. S13 (a1-c1) Cross-sectional view and (a2-c2) top view FCOM images of (a1-a2) SZ_air, (b1-b2) SZ_O_2, and (c1-c2) SZ_O_3. These images are identical to those shown in Fig. 3, while information of where the images were obtained is given here. In particular, orange dashed lines in (a1-c1) indicate the positions where the top view FCOM images in (a2-c2) were obtained. Likewise, orange dashed lines in (a2-c2) indicate the positions where the cross-sectional view FCOM images in (a1-c1) were obtained. For clarity, white dashed lines in (a1-c1) are added to indicate membrane outer surface (*upper*) and interface between the membrane and α-Al_2O_3 disc (*lower*).

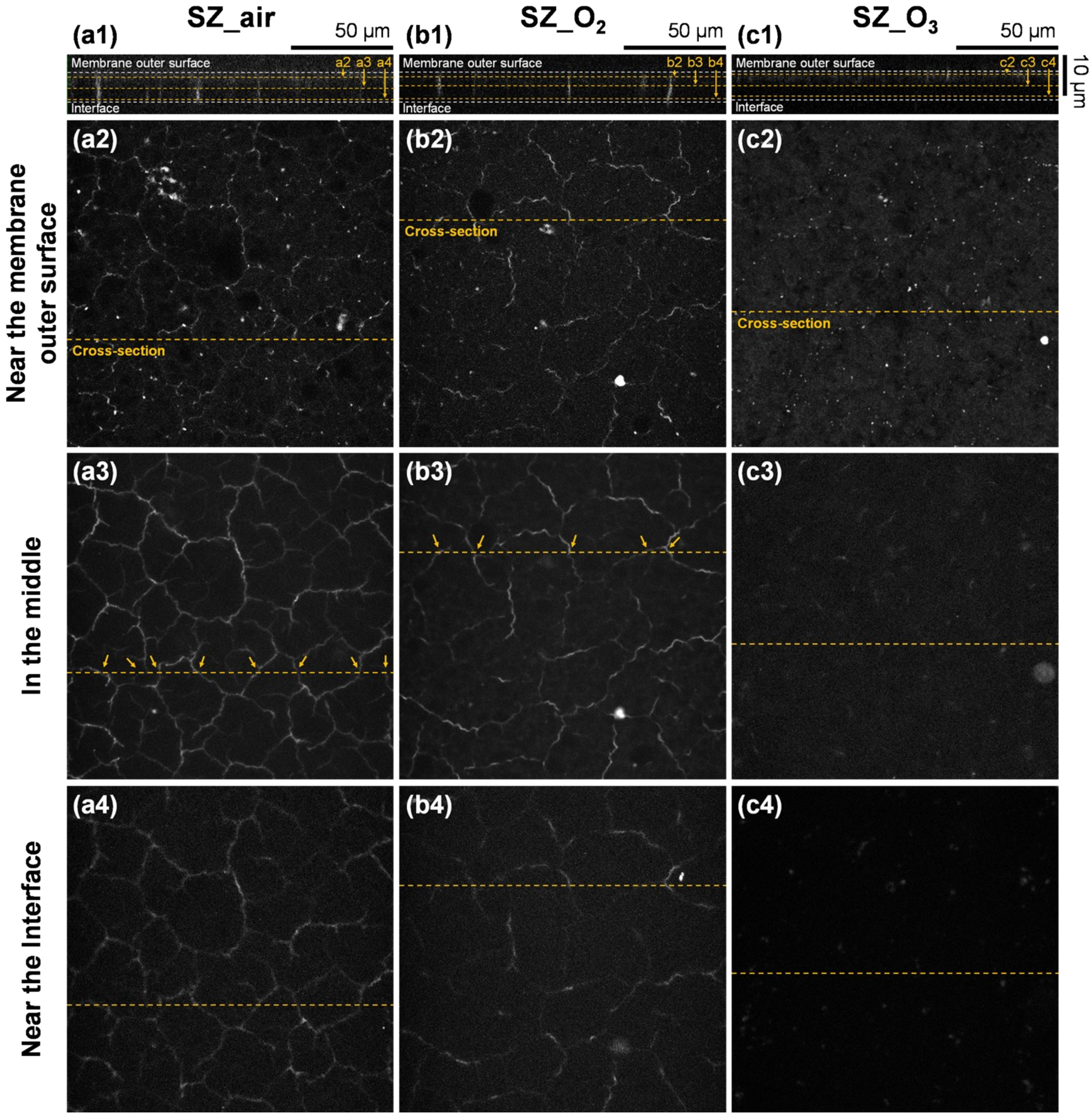

Fig. S14 FCOM images of (a1-a4) SZ_air, (b1-b4) SZ_O_2, and (c1-c4) SZ_O_3. Each membrane sample was dyed with 1 mM fluorescein sodium salt solution for 4 d. First row shows cross-sectional view FCOM images and second to fourth rows show top view FCOM images obtained (a2-c2) near the membrane outer surface, (a3-c3) in the middle, and (a4-c4) near the interface between the membrane and α-Al_2O_3 disc. Cross-sectional view FCOM images were obtained at areas indicated by orange dashed lines in top view FCOM images. Orange dashed lines in cross-sectional view FCOM images in (a1-c1) indicate positions of top view FCOM images shown in (*y*2-*y*4), where *y* = a, b, and c. White dashed lines in cross-sectional view FCOM images in (a1-c1) indicate the membrane outer surface and interface. For convenience, cracks shown in (a1, b1) are indicated by orange arrows in (a3, b3).

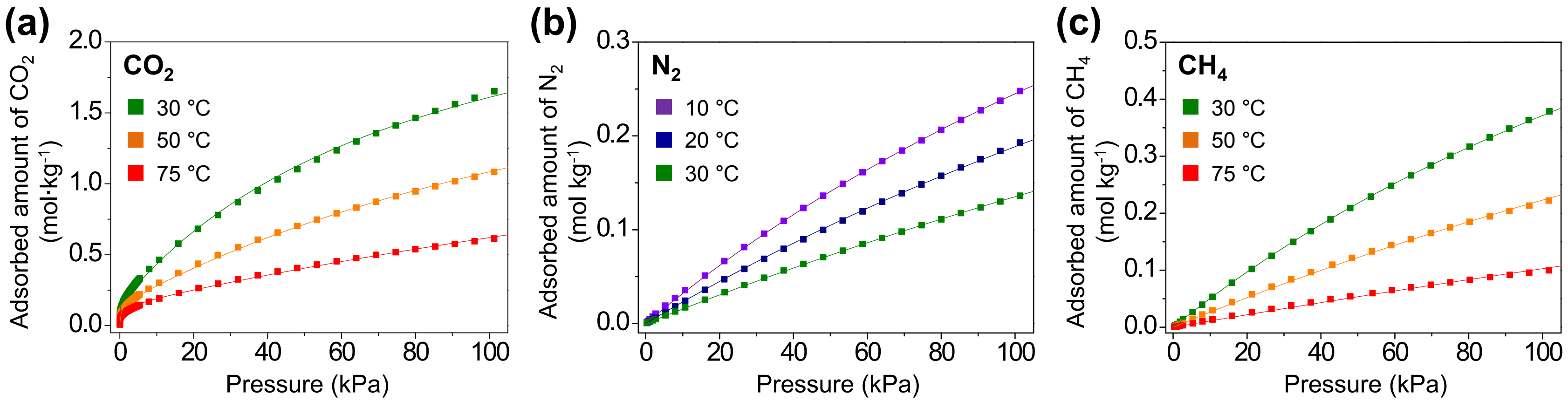

Fig. S15 Adsorption isotherms of (a) CO_2, (b) N_2, and (c) CH_4 in SZ-P_air. Adsorption isotherms of CO_2 and CH_4 in (a, c) were measured at 30, 50, and 75 °C, while that of N_2 in (b) was measured at 10, 20, and 30 °C. The fitted curves based on the parameters given in Table S1 are displayed as well.

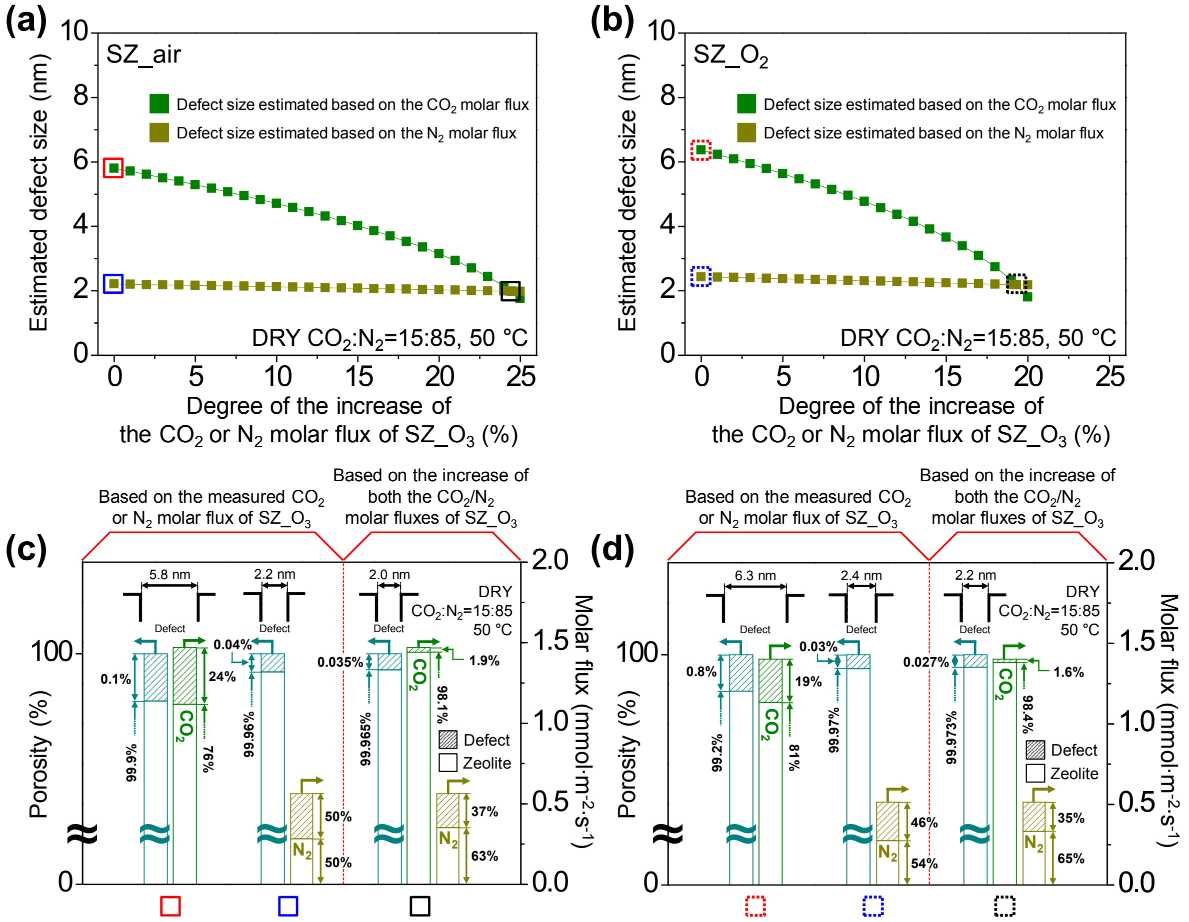

Fig. S16 Defect sizes for (a) SZ_air and (b) SZ_O_2 estimated by combining quantitative properties extracted from the FCOM images and unidimensional permeation modeling. To simulate intrinsic membrane performance, the CO_2 and N_2 molar fluxes of defect-free SZ_O_3 were equally increased, while preserving the corresponding CO_2/N_2 SF. (c, d) Porosities of defective and zeolitic parts and their corresponding contributions to the total CO_2 and N_2 molar fluxes of (c) SZ_air and (d) SZ_O_2 for CO_2/N_2 binary mixture feed composed of 15% CO_2 and 85% N_2 at 50 °C. Results corresponding to points marked by red, blue, and black boxes in (a) and dashed boxes in (b) are displayed in (c, d), respectively.

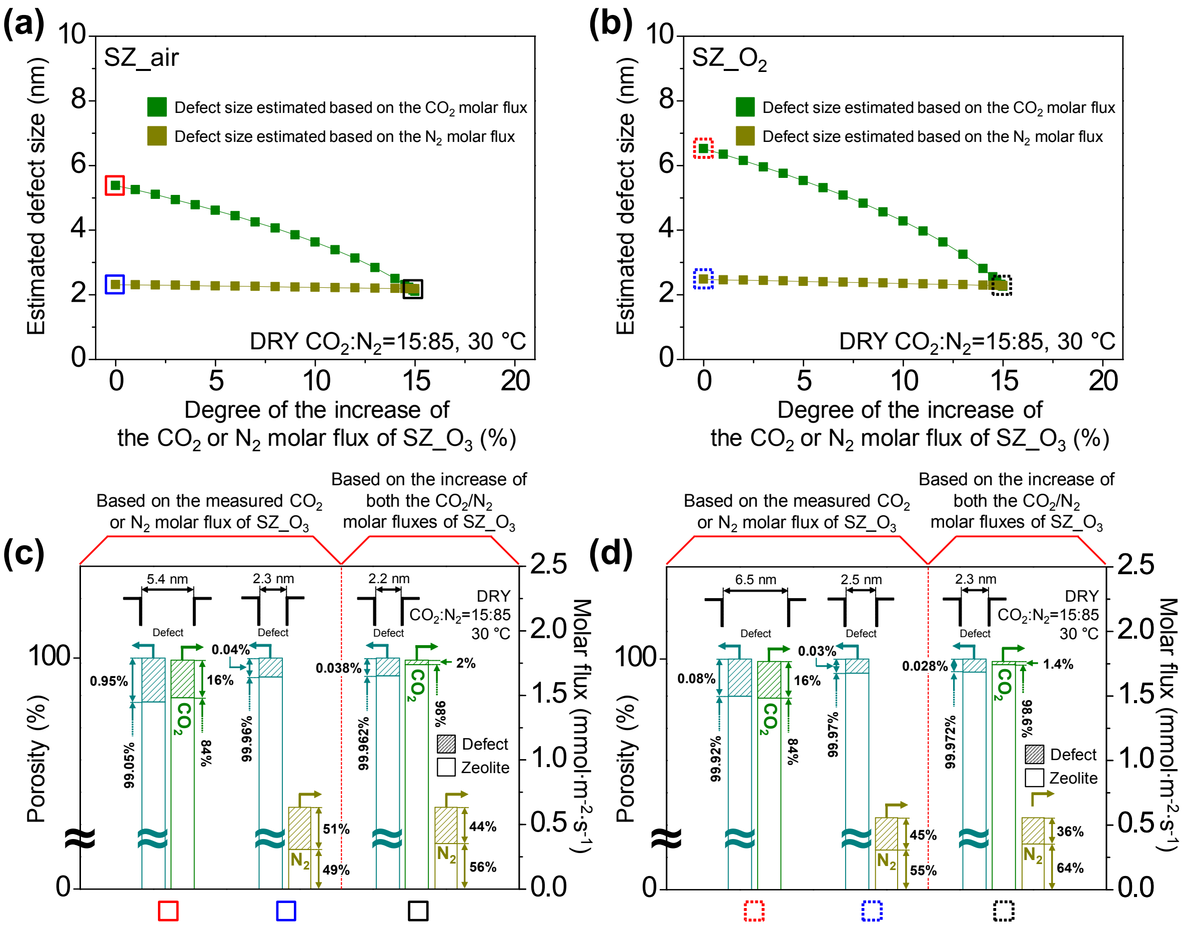

Fig. S17 Defect sizes for (a) SZ_air and (b) SZ_O_2 estimated by combining quantitative properties extracted from the FCOM images and unidimensional permeation modeling. To simulate intrinsic membrane performance, the CO_2 and N_2 molar fluxes of defect-free SZ_O_3 were equally increased, while preserving the corresponding CO_2/N_2 SF. (c, d) Porosities of defective and zeolitic parts and their corresponding contributions to the total CO_2 and N_2 molar fluxes of (c) SZ_air and (d) SZ_O_2 for CO_2/N_2 binary mixture feed composed of 15% CO_2 and 85% N_2 at 30 °C. Results corresponding to points marked by red, blue, and black boxes in (a) and dashed boxes in (b) are displayed in (c, d), respectively.

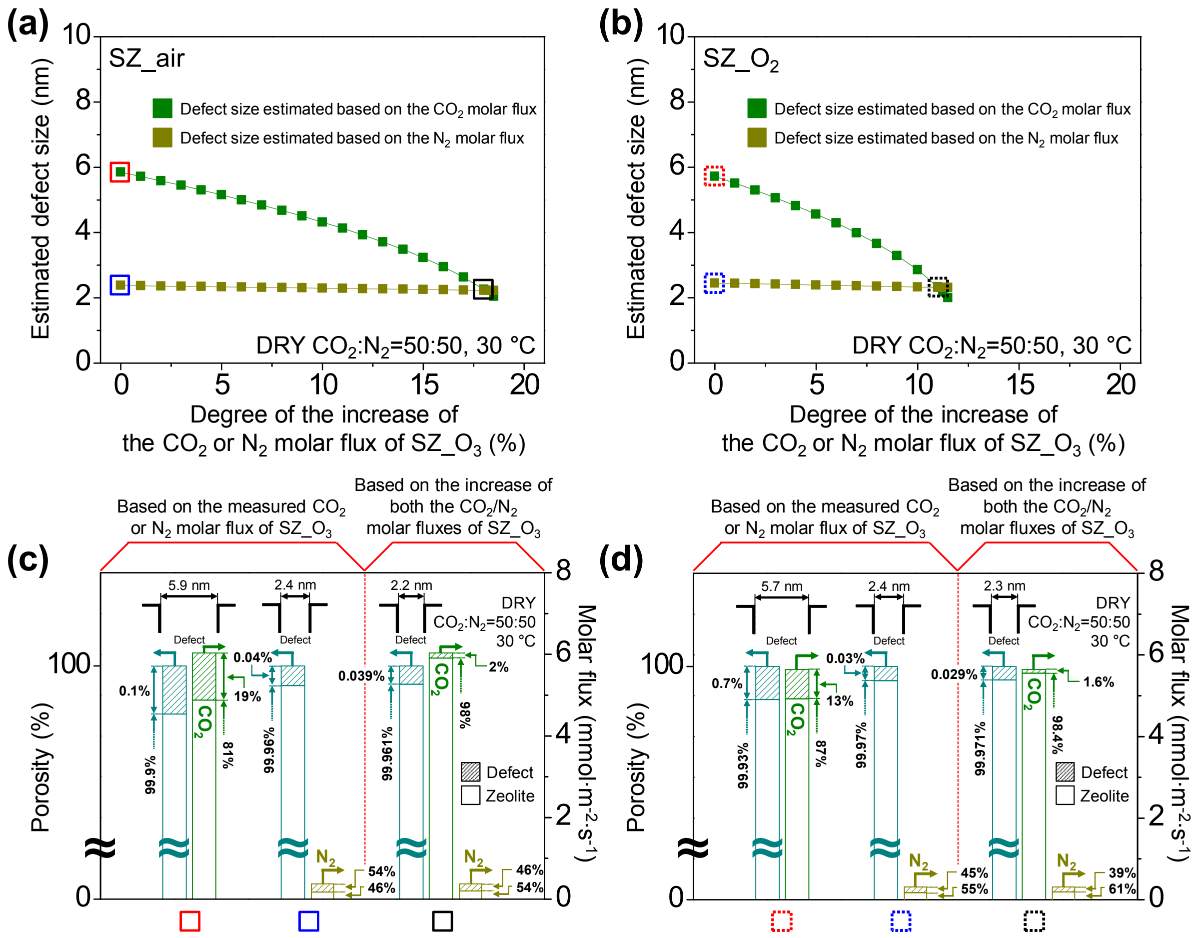

Fig. S18 Defect sizes for (a) SZ_air and (b) SZ_O_2 estimated by combining quantitative properties extracted from the FCOM images and unidimensional permeation modeling. To simulate intrinsic membrane performance, the CO_2 and N_2 molar fluxes of defect-free SZ_O_3 were equally increased, while preserving the corresponding CO_2/N_2 SF. (c, d) Porosities of defective and zeolitic parts and their corresponding contributions to the total CO_2 and N_2 molar fluxes of (c) SZ_air and (d) SZ_O_2 for equimolar CO_2/N_2 binary mixture feed at 30 °C. Results corresponding to points marked by red, blue, and black boxes in (a) and dashed boxes in (b) are displayed in (c, d), respectively.

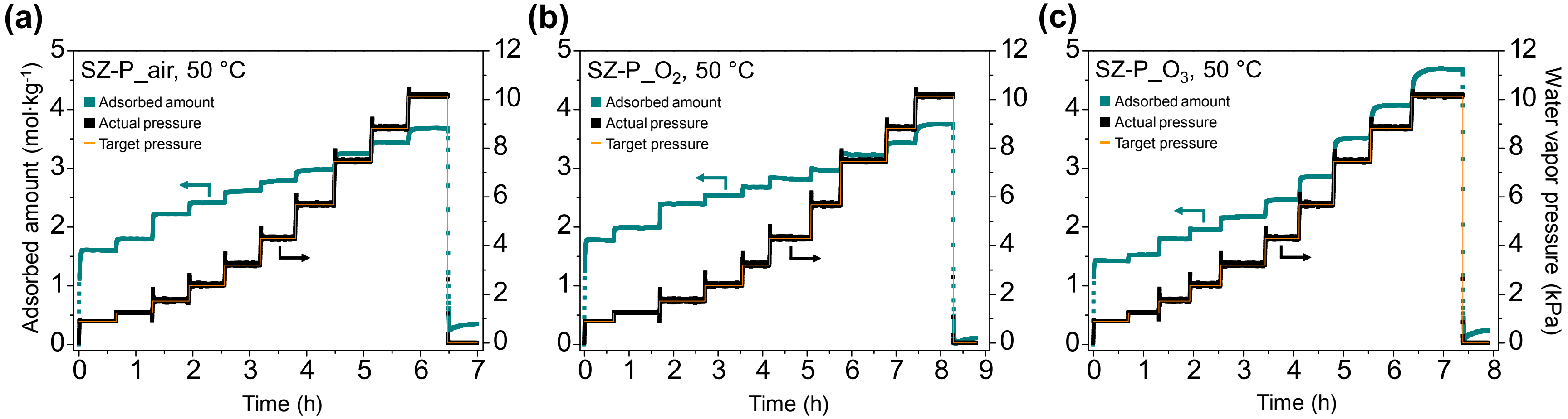

Fig. S19 Water vapor uptakes (*cyan*) in (a) SZ-P_air, (b) SZ-P_O_2, and (c) SZ-P_O_3 measured at different water vapor pressures (0.9, 1.2, 1.7, 2.3, 3.2, 4.2, 5.7, 7.4, 8.8, and 12.3 kPa) and 50 °C. In (a-c), target (*orange*) and actual (*black*) water vapor pressures are also displayed.

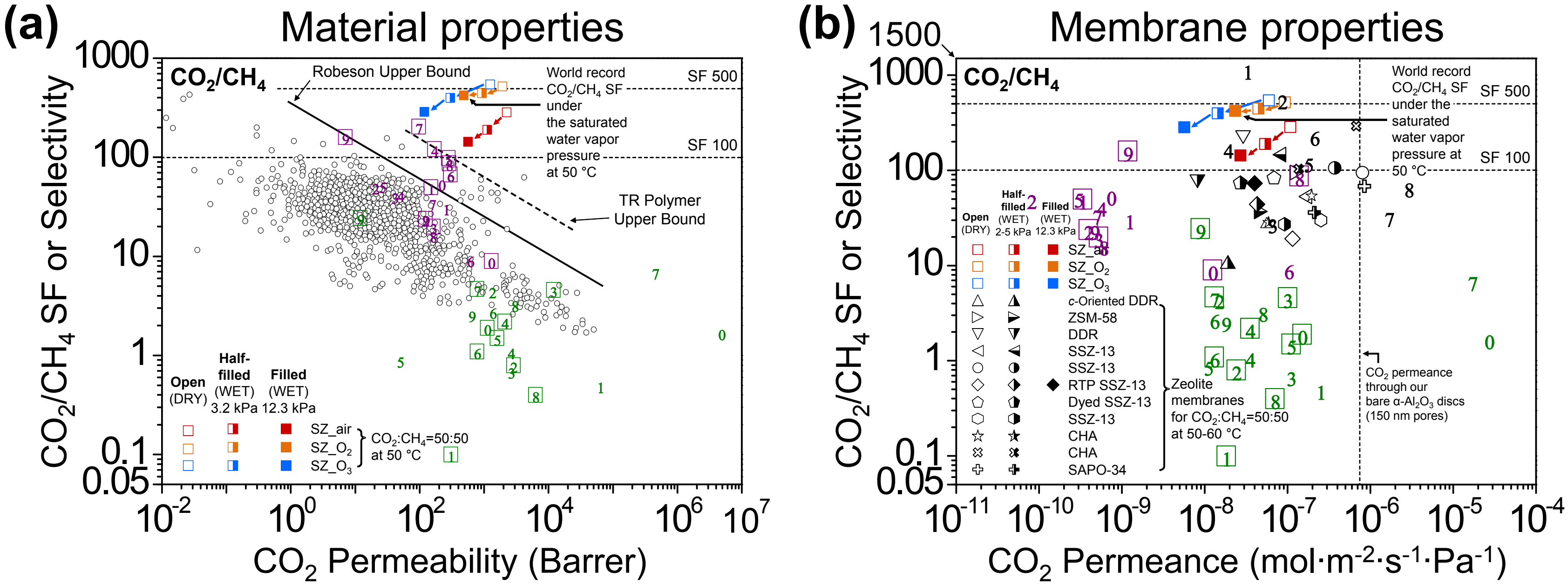

Zeolite membranes

□◧■	SZ_air	***Our work***
□◧■	SZ_O$_2$	
□◧■	SZ_O$_3$	
△◭	*c*-oriented DDR	Jang et al., *J. Chem. Mater. A*, **2020**. 28, 14071-14071
▷▶	ZSM-58	Kim et al., *J. Chem. Mater. A*, **2017**, 5, 11246-11254
▽▼	DDR	Wang et al., *J. Membr. Sci.*, **2017**, 539, 152-160
◁◀	SSZ-13	Lee et al, *J. Membr. Sci.*, **2020**. 611, 118390
○◐	SSZ-13	
◇⬖◆	RTP SSZ-13	Kim et al., *J. Membr. Sci.*, **2019**, 591, 117342
⬠⬟	Dyed SSZ-13	Hong et al., *Chem. Mater.*, **2018**, 30, 3346-3358
⬡⬢	SSZ-13	Kosinov et al., *J. Mater. Chem. A*, **2014**, 2, 13083-13092
☆★	CHA	Lee et al, *ACS Appl. Mater. Interfaces*, **2019**, 11, 3946-3960
✕✖	CHA	Zhou et al., *Energy Fuels*, **2020**, 34, 11307-11314
✛✚	SAPO-34	Chen et al., *J. CO$_2$. Util.*, **2017**, 18, 30-40
1	AlPO-18	Le et al., *ChemSusChem.*, **2020**, 13, 1720-1724
2	SAPO-34	
3	SDA-free CHA	Jang et al., *J. Membr. Sci.*, **2018**, 549, 46-59
4	SSZ-13	Wu et al., *J. Membr. Sci.*, **2015**, 473, 201-209
5	DDR	Himeno et al., *Ind. Eng. Chem. Res.*, **2007**, 46, 6989-6997
6	SAPO-34	Li et al., *Ind. Eng. Chem. Res.*, **2005**, 44, 3220-3228
7	CHA	Kida et al., *Sep. Purif. Technol.*, **2018**, 197, 116-121
8	AlPO-18	Wang et al., *J. Mater. Chem. A.*, **2019**, 7, 13164-13172

MOF membranes (DRY)

0	Cu$_3$(BTC)$_2$ MOF	Guo et al., *J. Am. Chem. Soc.*, **2009**, 131, 1646-1647
1	MOF-5	Liu et al., *Microporous Mesoporous Mater.*, **2009**, 118, 296-301
2	MOF-[Cu$_2$L$_2$P]$_n$	Bètard et al., *Microporous Mesoporous Mater.*, **2012**, 150, 76-82
3	MIL-53	Hu et al., *Chem. Commun.*, **2011**, 47, 737-739
4	SIM-1	Aguado et al., *New J. Chem.*, **2011**, 35, 41-44
5	ZIF-7	Li et al., *Angew. Chem. Int. Ed.*, **2010**, 49, 548-551
6	ZIF-8	Bux et al., *J. Am. Chem. Soc.*, **2009**, 131, 16000-16001
7	ZIF-8	S. R. Venna & M. A. Carreon, *J. Am. Chem. Soc.*, **2010**, 132, 76-78
8	ZIF-8	McCarthy et al., *Langmuir*, **2010**, 26, 14636-14641
9	ZIF-8	Bux et al., *Chem. Mater.*, **2011**, 23, 2262-2269
$\boxed{0}$	ZIF-8	Pan et al., *Chem. Commun.,* **2011**, 47, 10275-10277
$\boxed{1}$	ZIF-8	Xu et al., *J. Membr. Sci.*, **2011**, 385-386, 187-193
$\boxed{2}$	ZIF-22	Huang et al., *Angew. Chem. Int. Ed.*, **2010**, 49, 4958-4961
$\boxed{3}$	ZIF-69	Liu et al., *J. Membr. Sci.*, **2011**, 379, 46-51
$\boxed{4}$	ZIF-90	Huang et al., *J. Am. Chem. Soc.*, **2010**, 132, 15562-15564
$\boxed{5}$	ZIF-90	Brown et al., *Angew. Chem. Int. Ed.*, **2012**, 51, 10615-10618
$\boxed{6}$	ZIF-90	Huang et al., *Angew. Chem. Int. Ed.*, **2011**, 50, 4979-4982
$\boxed{7}$	ZIF-90	Huang et al., *Microporous Mesoporous Mater.*, **2014**, 192, 18-22
$\boxed{8}$	ZIF-95	Huang et al., *Chem. Commun.*, **2012**, 48, 10981-10983
$\boxed{9}$	ZIF-7$_{22}$-8	Hou et al., *Angew. Chem. Int. Ed.*, **2019**, 58, 327-331

Carbon & mixed-matrix membranes (DRY)

0	Xiang et al., *Adv, Mater.*, **2017**, 29, 1606999
1	M. S. Boroglu & A. B. Yumru, *Sep. Purif. Technol.*, **2017**, 173, 269-279
2	Anson et al., *J. Membr. Sci.*, **2004**, 243, 19-28
3	Nik et al., *J. Membr. Sci.*, **2011**, 379, 468-478
4	Nik et al. *J. Membr. Sci.*, **2012**, 413-414, 48-61
5	
6	Jomekian et al., *J. Nat. Gas Sci. Eng.*, **2016**, 31, 562-574
7	Rabiee et al., *J. Ind. Eng. Chem.*, **2015**, 27, 223-239
8	Wang et al., *J. Membr. Sci.*, **2014**, 460, 62-70
9	Zhou et al., *J. Membr. Sci.*, **2015**, 489, 1-10
$\boxed{0}$	Nafisi et al., *J. Membr. Sci.*, **2014**, 459, 244-255
$\boxed{1}$	Rahman et al., *J. Membr. Sci.*, **2013**, 437, 286-297
$\boxed{2}$	Meshkat et al., *Sep. Purif. Technol.*, **2018**, 200, 177-190
$\boxed{3}$	
$\boxed{4}$	Hosseini and T. S. Chung, *J. Membr. Sci.*, **2009**, 328, 174-185
$\boxed{5}$	
$\boxed{6}$	
$\boxed{7}$	
$\boxed{8}$	Ismail et al., *Chem. Eng. Trans.*, **2015**, 45, 1465-1470
$\boxed{9}$	Centeno et al., *J. Membr. Sci.*, **1999**, 160, 201-211

Fig. S20 (a) CO_2/CH_4 SFs (or selectivities) vs. CO_2 permeabilities of SZ_air (*red*), SZ_O_2 (*orange*), and SZ_O_3 (*blue*) under dry conditions (*open*) and wet conditions (ca. 3.2 kPa (*half-filled*) and 12.3 kPa (*filled*)) at 50 °C. For comparison, the performances of polymeric (○),[16] metal organic framework (MOF) (*green*),[27-46] and carbon & mixed-matrix (*purple*)[47-61] membranes under dry conditions are included. In addition, Robeson and thermally rearranged (TR) polymer upper bounds are denoted by black solid and dashed lines, respectively.[16] (b) CO_2/CH_4 SFs (or selectivities) vs. CO_2 permeances of the SZ membrane series and other zeolite membranes (*marked by symbol*)[10, 12, 17-21, 62-64] measured at 50-60 °C under dry conditions (*open for symbols*) and wet conditions (ca. 2-5 kPa (*half-filled*) and 12.3 kPa (*filled*)). For comparison, the performances of additional zeolite (*numbered*),[23, 65-70] MOF (*green*),[27-46] and carbon & mixed-matrix (*purple*)[47-49, 51-58, 60, 61] membranes under dry conditions are included. Horizontal dashed lines in (a, b) indicate CO_2/CH_4 SFs of 100 and 500. A vertical dashed line in (b) indicates CO_2 permeance estimated through Knudsen diffusion of a bare α-Al_2O_3 disc having 150 nm pores. Detailed information about the membranes used for the graphs is described below.

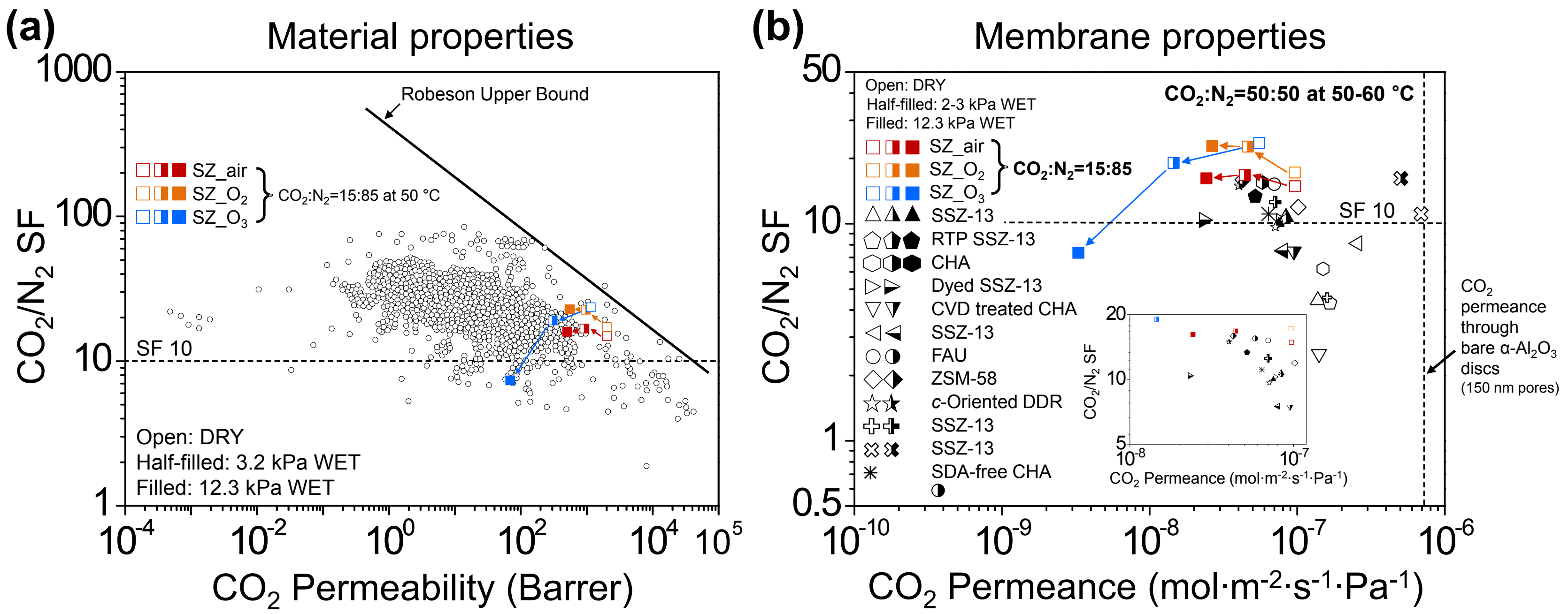

Fig. S21 (a) CO_2/N_2 SFs vs. CO_2 permeabilities of SZ_air (*red*), SZ_O_2 (*orange*), and SZ_O_3 (*blue*) under dry conditions (*open*) and wet conditions (ca. 3.2 kPa (*half-filled*) and 12.3 kPa (*filled*)) at 50 °C. In (a), for comparison, the performances of polymeric membranes (*open dots*) and Robeson upper bound is denoted by the black line.[16] (b) CO_2/N_2 SFs vs. CO_2 permeances of the SZ membrane series and other zeolite membranes[10, 12, 17-24] measured at 50-60 °C under dry conditions (*open*) and wet conditions (ca. 2-3 kPa (*half-filled*) and 12.3 kPa (*filled*)). In (b), for clarity, the concentrated part of separation performances is illustrated in the inset graph. Horizontal dashed lines in (a, b) indicate the CO_2/N_2 SF of 10, while a vertical dashed line in (b) indicates CO_2 permeance through Knudsen diffusion of a bare α-Al_2O_3 disc having 150 nm pores.

References

1. Y. Jeong, S. Hong, E. Jang, E. Kim, H. Baik, N. Choi, A. C. K. Yip and J. Choi, *Angew. Chem. Int. Ed.*, 2019, **58**, 18654-18662.
2. J. Kuhn, J. Gascon, J. Gross and F. Kapteijn, *Microporous Mesoporous Mater.*, 2009, **120**, 12-18.
3. D. M. D'Alessandro, B. Smit and J. R. Long, *Angew. Chem. Int. Ed.*, 2010, **49**, 6058-6082.
4. R. Balasubramanian and S. Chowdhury, *J. Mater. Chem. A*, 2015, **3**, 21968-21989.
5. T. C. Merkel, H. Q. Lin, X. T. Wei and R. Baker, *J. Membr. Sci.*, 2010, **359**, 126-139.
6. D. Singh, E. Croiset, P. L. Douglas and M. A. Douglas, *Energy Convers. Manag.*, 2003, **44**, 3073-3091.
7. J. Choi, H. K. Jeong, M. A. Snyder, J. A. Stoeger, R. I. Masel and M. Tsapatsis, *Science*, 2009, **325**, 590-593.
8. N. Hedin, G. J. DeMartin, W. J. Roth, K. G. Strohmaier and S. C. Reyes, *Microporous Mesoporous Mater.*, 2008, **109**, 327-334.
9. T. Lee, J. Choi and M. Tsapatsis, *J. Membr. Sci.*, 2013, **436**, 79-89.
10. S. Hong, D. Kim, Y. Jeong, E. Kim, J. C. Jung, N. Choi, J. Nam, A. C. K. Yip and J. Choi, *Chem. Mater.*, 2018, **30**, 3346-3358.
11. S. Hong, D. Kim, H. Richter, J. H. Moon, N. Choi, J. Nam and J. Choi, *J. Membr. Sci.*, 2019, **569**, 91-103.
12. J. Kim, E. Jang, S. Hong, D. Kim, E. Kim, H. Ricther, A. Simon, N. Choi, D. Korelskiy, S. Fouladvand, J. Nam and J. Choi, *J. Membr. Sci.*, 2019, **591**, 117342.
13. J. Kuhn, J. M. Castillo-Sanchez, J. Gascon, S. Calero, D. Dubbeldam, T. J. H. Vlugt, F. Kapteijn and J. Gross, *J. Phys. Chem. C*, 2009, **113**, 14290-14301.
14. M. Pan and Y. S. Lin, *Microporous Mesoporous Mater.*, 2001, **43**, 319-327.
15. J. Hedlund, J. Sterte, M. Anthonis, A. J. Bons, B. Carstensen, N. Corcoran, D. Cox, H. Deckman, W. De Gijnst, P. P. de Moor, F. Lai, J. McHenry, W. Mortier and J. Reinoso, *Microporous Mesoporous Mater.*, 2002, **52**, 179-189.
16. L. M. Robeson, *J. Membr. Sci.*, 2008, **320**, 390-400.
17. E. Kim, S. Hong, E. Jang, J. H. Lee, J. C. Kim, N. Choi, C. H. Cho, J. Nam, S. K. Kwak, A. C. K. Yip and J. Choi, *J. Mater. Chem. A*, 2017, **5**, 11246-11254.
18. E. Jang, J. H. Lee, S. Hong, Y. Jeong, J. C. Kim, D. Kim, H. Baik, E. Kim, N. Choi, J. Nam, S. J. Cho, S. K. Kwak and J. Choi, *J. Mater. Chem. A*, 2020, **8**, 14071-14081.
19. N. Kosinov, C. Auffret, C. Gucuyener, B. M. Szyja, J. Gascon, F. Kapteijn and E. J. M. Hensen, *J. Mater. Chem. A*, 2014, **2**, 13083-13092.
20. M. Lee, Y. Jeong, S. Hong and J. Choi, *J. Membr. Sci.*, 2020, **611**, 118390.
21. M. Lee, S. Hong, D. Kim, E. Kim, K. Lim, J. C. Jung, H. Richter, J. H. Moon, N. Choi, J. Nam and J. Choi, *ACS Appl. Mater. Interfaces*, 2019, **11**, 3946-3960.
22. E. Kim, T. Lee, H. Kim, W. J. Jung, D. Y. Han, H. Baik, N. Choi and J. Choi, *Environ. Sci. Technol.*, 2014, **48**, 14828-14836.
23. E. Jang, S. Hong, E. Kim, N. Choi, S. J. Cho and J. Choi, *J. Membr. Sci.*, 2018, **549**, 46-59.

24. X. H. Gu, J. H. Dong and T. M. Nenoff, *Ind. Eng. Chem. Res.*, 2005, **44**, 937-944.
25. J. van den Bergh, W. Zhu, J. Gascon, J. A. Moulijn and F. Kapteijn, *J. Membr. Sci.*, 2008, **316**, 35-45.
26. P. M. Mathias, R. Kumar, J. D. Moyer, J. M. Schork, S. R. Srinivasan, S. R. Auvil and O. Talu, *Ind. Eng. Chem. Res.*, 1996, **35**, 2477-2483.
27. H. L. Guo, G. S. Zhu, I. J. Hewitt and S. L. Qiu, *J. Am. Chem. Soc.*, 2009, **131**, 1646-1647.
28. Y. Y. Liu, Z. F. Ng, E. A. Khan, H. K. Jeong, C. B. Ching and Z. P. Lai, *Microporous Mesoporous Mater.*, 2009, **118**, 296-301.
29. A. Betard, H. Bux, S. Henke, D. Zacher, J. Caro and R. A. Fischer, *Microporous Mesoporous Mater.*, 2012, **150**, 76-82.
30. Y. X. Hu, X. L. Dong, J. P. Nan, W. Q. Jin, X. M. Ren, N. P. Xu and Y. M. Lee, *Chem. Commun.*, 2011, **47**, 737-739.
31. S. Aguado, C. H. Nicolas, V. Moizan-Basle, C. Nieto, H. Amrouche, N. Bats, N. Audebrand and D. Farrusseng, *New J. Chem.*, 2011, **35**, 41-44.
32. Y. S. Li, F. Y. Liang, H. Bux, A. Feldhoff, W. S. Yang and J. Caro, *Angew. Chem. Int. Ed.*, 2010, **49**, 548-551.
33. H. Bux, F. Y. Liang, Y. S. Li, J. Cravillon, M. Wiebcke and J. Caro, *J. Am. Chem. Soc.*, 2009, **131**, 16000-16001.
34. S. R. Venna and M. A. Carreon, *J. Am. Chem. Soc.*, 2010, **132**, 76-78.
35. M. C. McCarthy, V. Varela-Guerrero, G. V. Barnett and H. K. Jeong, *Langmuir*, 2010, **26**, 14636-14641.
36. H. Bux, A. Feldhoff, J. Cravillon, M. Wiebcke, Y. S. Li and J. Caro, *Chem. Mater.*, 2011, **23**, 2262-2269.
37. Y. C. Pan, Y. Y. Liu, G. F. Zeng, L. Zhao and Z. P. Lai, *Chem. Commun.*, 2011, **47**, 2071-2073.
38. G. S. Xu, J. F. Yao, K. Wang, L. He, P. A. Webley, C. S. Chen and H. T. Wang, *J. Membr. Sci.*, 2011, **385**, 187-193.
39. A. S. Huang, H. Bux, F. Steinbach and J. Caro, *Angew. Chem. Int. Ed.*, 2010, **49**, 4958-4961.
40. Y. Y. Liu, G. F. Zeng, Y. C. Pan and Z. P. Lai, *J. Membr. Sci.*, 2011, **379**, 46-51.
41. A. S. Huang, W. Dou and J. Caro, *J. Am. Chem. Soc.*, 2010, **132**, 15562-15564.
42. A. J. Brown, J. R. Johnson, M. E. Lydon, W. J. Koros, C. W. Jones and S. Nair, *Angew. Chem. Int. Ed.*, 2012, **51**, 10615-10618.
43. A. S. Huang and J. Caro, *Angew. Chem. Int. Ed.*, 2011, **50**, 4979-4982.
44. A. S. Huang, Q. Liu, N. Y. Wang and J. Caro, *Microporous Mesoporous Mater.*, 2014, **192**, 18-22.
45. A. S. Huang, Y. F. Chen, N. Y. Wang, Z. Q. Hu, J. W. Jiang and J. Caro, *Chem. Commun.*, 2012, **48**, 10981-10983.
46. Q. Q. Hou, Y. Wu, S. Zhou, Y. Y. Wei, J. Caro and H. H. Wang, *Angew. Chem. Int. Ed.*, 2019, **58**, 327-331.
47. L. Xiang, L. Q. Sheng, C. Q. Wang, L. X. Zhang, Y. C. Pan and Y. S. Li, *Adv. Mater.*, 2017, **29**, 1606999.
48. M. S. Boroglu and A. B. Yumru, *Sep. Purif. Technol.*, 2017, **173**, 269-279.
49. M. Anson, J. Marchese, E. Garis, N. Ochoa and C. Pagliero, *J. Membr. Sci.*, 2004, **243**, 19-28.
50. O. G. Nik, X. Y. Chen and S. Kaliaguine, *J. Membr. Sci.*, 2011, **379**, 468-478.
51. O. G. Nik, X. Y. Chen and S. Kaliaguine, *J. Membr. Sci.*, 2012, **413**, 48-61.

52. A. Jomekian, R. M. Behbahani, T. Mohammadi and A. Kargari, *J. Nat. Gas Sci. Eng.*, 2016, **31**, 562-574.
53. H. Rabiee, S. M. Alsadat, M. Soltanieh, S. A. Mousavi and A. Ghadimi, *J. Ind. Eng. Chem.*, 2015, **27**, 223-239.
54. S. F. Wang, Y. Liu, S. X. Huang, H. Wu, Y. F. Li, Z. Z. Tian and Z. Y. Jiang, *J. Membr. Sci.*, 2014, **460**, 62-70.
55. T. T. Zhou, L. Luo, S. Hua, S. F. Wang, R. N. Zhang, H. Wu, Z. Y. Jiang, B. Y. Wang and J. Yang, *J. Membr. Sci.*, 2015, **489**, 1-10.
56. V. Nafisi and M. B. Hagg, *J. Membr. Sci.*, 2014, **459**, 244-255.
57. M. M. Rahman, V. Filiz, S. Shishatskiy, C. Abetz, S. Neumann, S. Bolmer, M. M. Khan and V. Abetz, *J. Membr. Sci.*, 2013, **437**, 286-297.
58. S. Meshkat, S. Kaliaguine and D. Rodrigue, *Sep. Purif. Technol.*, 2018, **200**, 177-190.
59. S. S. Hosseini and T. S. Chung, *J. Membr. Sci.*, 2009, **328**, 174-185.
60. N. H. Ismail, W. N. W. Salleh, N. Sazali and A. F. Ismail, *Chem. Eng. Trans.*, 2015, **45**, 1465-1470.
61. T. A. Centeno and A. B. Fuertes, *J. Membr. Sci.*, 1999, **160**, 201-211.
62. L. Wang, C. Zhang, X. C. Gao, L. Peng, J. Jiang and X. H. Gu, *J. Membr. Sci.*, 2017, **539**, 152-160.
63. Y. Chen, Y. T. Zhang, C. Zhang, J. Jiang and X. H. Gu, *J. CO_2 Util.*, 2017, **18**, 30-40.
64. J. J. Zhou, F. Gao, K. Sun, X. Y. Jin, Y. Zhang, B. Liu and R. F. Zhou, *Energy Fuels*, 2020, **34**, 11307-11314.
65. Q. T. Le, D. H. P. Nguyen, N. M. Nguyen, D. P. H. Nguyen, T. M. Nguyen, T. N. Nguyen and T. C. T. Pham, *ChemSusChem*, 2020, **13**, 1720-1724.
66. T. Wu, M. C. Diaz, Y. Zheng, R. Zhou, H. H. Funke, J. L. Falconer and R. D. Noble, *J. Membr. Sci.*, 2015, **473**, 201-209.
67. S. Himeno, T. Tomita, K. Suzuki, K. Nakayama, K. Yajima and S. Yoshida, *Ind. Eng. Chem. Res.*, 2007, **46**, 6989-6997.
68. S. G. Li, J. G. Martinek, J. L. Falconer, R. D. Noble and T. Q. Gardner, *Ind. Eng. Chem. Res.*, 2005, **44**, 3220-3228.
69. K. Kida, Y. Maeta and K. Yogo, *Sep. Purif. Technol.*, 2018, **197**, 116-121.
70. B. Wang, F. Gao, F. Zhang, W. H. Xing and R. F. Zhou, *J. Mater. Chem. A*, 2019, **7**, 13164-13172.